An Improved Self-Consistent Approach to Attenuation Correction for C-band Polarimetric Radar Measurements and Its Impact on Quantitative Precipitation Estimation

Yabin Gou[a,b], Haonan Chen[c,d*], and Jiafeng Zheng[e*]

[a]*Hangzhou Meteorological Bureau, Hangzhou 310051, China*

[b]*Zhejiang Institute of Meteorological Sciences, Hangzhou 321000, China*

[c]*Physical Sciences Division, NOAA/Earth System Research Laboratory, Boulder, CO 80305, USA*

[d]*Cooperative Institute for Research in the Atmosphere, Colorado State University, Fort Collins, CO 80523, USA*

[e]*School of Atmospheric Sciences, Chengdu University of Information Technology, Chengdu, 610225, China*

Manuscript Submitted to *Atmospheric Research*

Accepted: 1 March 2019

Corresponding author address: *Haonan Chen, NOAA/ESRL Physical Sciences Division, 325 Broadway, Boulder, CO 80305, USA. E-mail address:* haonan.chen@noaa.gov; *Dr. Jiafeng Zheng,*

No 24 section 1, Xuefu road, Chengdu, China, E-mail address: zjf1988@cuit.edu.cn.

Abstract

Attenuation correction of measured reflectivity (Z_{H}) and differential reflectivity (Z_{DR}) is critical in short-wavelength radar applications, especially during extreme precipitation events such as heavy rain. This paper develops an improved self-consistent approach (improved ZPHI method) for attenuation correction in practical environment. In particular, a non-negative constraint is imposed on the specific attenuation, which is inferred from the monotonic increasing characteristic of differential propagation phase (Φ_{DP}). The copolar correlation coefficient (ρ_{HV}) is used to partition the Φ_{DP} profiles into independent range segments, which are featured by different hydrometeor phases such as liquid rain or mixed-phase precipitation. Additional minimization constraint is imposed on the cost function of the difference between preprocessed Φ_{DP} and reconstructed Φ_{DP} to ensure its appropriate convergence. In addition, an exponential $Z_{\mathrm{DR}} - Z_{\mathrm{H}}$ relation derived from local raindrop size distribution (DSD) data is applied in the procedure of Z_{DR} correction. Polarimetric measurements from a C-band radar (CPOL) in Hangzhou of China during two extreme precipitation events are used to demonstrate the improved attenuation correction method. DSD observations from disdrometers and radar data from a nearby system operating at non-attenuated frequency (i.e., S-band) at Huangshan Mountain are used to evaluate the attenuation correction performance. This paper also studies the impact of attenuation correction on the radar-derived quantitative precipitation estimation (QPE) product, through cross-comparison with rain gauge observations. Results show that the polarimetric observations from CPOL radar are effectively enhanced and more consistent with collocated S-band measurements and the simulated radar moments based on DSD data. Hourly

rainfall products derived from $R(Z_{\mathrm{H}})$ and $R(Z_{\mathrm{H}}, Z_{\mathrm{DR}})$ are significantly improved, which are comparable to $R(K_{\mathrm{DP}})$ after attenuation correction.

Key words: C-band, polarimetric radar, attenuation correction, quantitative precipitation estimation.

1. Introduction

Dual-polarization weather radars have been widely used to study the microphysical characteristics of precipitation and quantify the precipitation rate and amount. Ground-based dual-polarization radar systems also form the cornerstones of national severe weather warning and forecast infrastructure in many countries. The operational dual-polarization radars in the U.S. are S band (~3GHz) systems whereas C-band (~5.5GHz) systems are generally deployed in Europe. In China, 216 weather radars are deployed to construct the China New Generation Weather Radar (CINRAD) network. Among them, 122 are S-band systems and they are mainly deployed in eastern China; 94 are C-band systems and they are mainly deployed in the western regions. Considering the demonstrated superior performance of dual-polarization radar, large-scale dual-polarization upgrade is being planned in China for the next few years. In addition, a third class of systems is emerging in urban areas where X-band (~9.4GHz) radar networks are being deployed operationally (e.g., Chandrasekar et al., 2012; Chandrasekar et al., 2018; Lim et al., 2018). The smaller, short-range, X-band systems can also be used to fill the gaps between S- and C-band weather radar sites, especially in complex terrain (Chen et al., 2017b; Cifelli et al., 2018). However, the high frequency signals at C- or X-band (or even higher) severely suffer from attenuation due to the propagation in rain (Bringi et al., 2001; Ryzhkov et al., 2014; Park et al., 2005; Gorgucci et al., 2006; Islam et al., 2014; Shimamura et al., 2016; Lim and Chandrasekar, 2016). The attenuation effect is especially significant

during the convective storm events in the summer flood seasons in China. Hence, attenuation correction of reflectivity Z_{H} and differential reflectivity Z_{DR} is indispensable in the quantitative applications of short wavelength polarimetric radars, such as raindrop size distribution (DSD) parameter retrievals (Wen et al., 2018), identification of different hydrometeor phases (Park et al., 2009; Chandrasekar et al., 2013), quantitative precipitation estimation and forecast (QPE/QPF) (Gorgucci and Baldini, 2015; Chen et al., 2017a; Gou et al., 2019), and timely nowcast of precipitation-related hazards (Chen and Chandrasekar, 2018).

The most important basis for attenuation correction is the self-consistency between polarimetric radar variables and the fact that the differential propagation phase (total phase Ψ_{DP} or filtered phase Φ_{DP}, deg) and derived specific differential phase (K_{DP}, deg·km^{-1}) are immune to attenuation. The conventional attenuation correction method (i.e., ZPHI method: Testud et al., 2000; Bringi et al., 2001) utilized the self-consistent constraints imposed on Φ_{DP} to derive specific attenuation A_{H} and differential attenuation A_{DP}. Park et al. (2005) further extended the ZPHI method from C-band application in Bringi et al. (2001) to X-band frequency. Therein, various parametric relations of X-band polarimetric observables are taken into account. Gorgucci et al. (2006) utilized the self-consistent relations between K_{DP} and Z_{H} and Z_{DR} to indirectly and iteratively derive A_{H} and A_{DP}, where the drop shape model and size distributions are critical in their implementation. However， the assumption of a linear shape size model in Gorgucci et al. (2000) may not be sufficient to represent the distribution in real environment. Lim and Chandrasekar (2006, 2016) have proposed a more complex rainfall profiling system for attenuation correction, which is not affected by the measurement bias of Z_{H} and Z_{DR}. Their multi-step process can also incorporate more theoretical models to

estimate the optimal relations between polarimetric radar variables at different drop shape and temperature conditions (Lim and Chandrasekar, 2016). However, this approach is mathematically complex and the computational cost is too high for real-time implementation. In addition, though the abovementioned approaches worked well for simulation data, more practical considerations should be taken into account in operational environment. In practical applications, the ZPHI method can be easily implemented but it is seriously affected by the non-monotonic behavior of measured Ψ_{DP}, which can be attributed to the backscatter differential phase (δ; deg) caused by Mie scattering of the irregular hail stones, big rain drops or the melting layers with wet snowflakes. The nonuniform beam filling effect with mixed-phase hydrometeors along Ψ_{DP} range profile (Zrnic et al., 1993; Ryzhkov and Zrnic, 1998; Ryzhkov 2007) is another issue that hinders the real application of the ZPHI method. Ideally, the total propagation path should be divided into different parts in order to incorporate the variations of hydrometeor phase. Traditionally, the iterative filtering techniques, such as the finite-impulse response (FIR) filter, can be applied to detect and remove the δ bumps from measured Ψ_{DP} profile (Hubbert et al., 1993; Hubbert and Bingi, 1995). Recently, Schneebeli and Berne (2012) and Schneebeli et al. (2014) attempted to use Kalman filtering to process Ψ_{DP} using the consistency between various polarimetric variables. Both methods aimed to separate δ from Φ_{DP} according to

$$\Psi_{DP} = \delta + \Phi_{DP}(r) = \delta + 2\int_0^r \alpha K_{DP}(s)ds = \delta + 2\int_0^r A_H(s)ds \quad (1)$$

where α is the coefficient relating K_{DP} to A_H in a linear relation and its value ranges from 0.03 to 0.18 at C-band, which should be optimally searched in the ZPHI processing chain (Bringi et al., 2001).

However, it should be noted that the FIR filter pattern may lose its potential capability if a large number of big drops, rain-hail or rain-ice mixtures still exist along the filtered Φ_{DP} profiles, which

can produce significant δ bumps extending over many consecutive range gates (Hubbert and Bringi, 1995). The relations between different polarimetric moments applied in the Kalman filtering greatly rely on the assumption of gamma function of DSD, which may not be suitable in many other precipitation regimes (Schneebeli and Berne, 2012). This paper develops an improved attenuation correction scheme based on traditional ZPHI method with more emphasis on the practical implementations. The improved approach incorporates more physical constraints, including: 1) the non-negative property of A_{H}; 2) the fact that low ρ_{HV} is always associated with non-liquid hydrometeors (Trömel et al., 2013; 2014); 3) the convergence constraint on the cost function of reconstructed Φ_{DP}; and 4) an exponential $Z_{\mathrm{DR}} - Z_{\mathrm{H}}$ relation derived from local DSD measurements. All these are considered priori knowledge and integrated into the ZPHI processing chain to improve the estimation of A_{H} and A_{DP} along the whole Φ_{DP} range profile.

The improved ZPHI method is demonstrated using C-band polarimetric (hereafter referred to CPOL) radar observations in Hangzhou, China. The CPOL radar, maintained by Hangzhou meteorological bureau, is the first C-band dual-polarization radar routinely operating in China. In addition, the urban area covered by the CPOL radar is one of the most prosperous economies in China. This operational polarimetric radar observations and products are used by local forecasters and emergency managers for urban hazard monitoring and decision making. Therefore, this paper takes this opportunity to report some of the first and detailed polarimetric radar observations and technical progress in China. The impact of the improved attenuation correction approach on radar QPE is also investigated.

This paper is organized as follows. Section 2 presents the improved attenuation correction

methodology based on the self-consistency criterion. Section 3 describes the dataset collected by the CPOL radar and demonstrates the attenuation correction performance. The impacts of attenuation correction on radar QPE are detailed in Section 4. Section 5 summarizes the main findings of this study.

2. Improved self-consistent approach to attenuation correction

2.1. Background of the ZPHI method

The main concept of the ZPHI method (Testud et al., 2000; Bringi et al., 2001) is illustrated by Eqs. 2a-2g:

$$A_{\mathrm{H}}(r) = \frac{[Z_{\mathrm{H}}^{\mathrm{M}}]^b[10^{0.1b\alpha\Delta\Phi(r_0,r_m)}-1]}{I(r_0,r_m)+[10^{0.1b\alpha\Delta\Phi(r_0,r_m)}-1]I(r,r_m)} \quad (2a)$$

$$\Delta\Phi_{\mathrm{DP}}^{\mathrm{filtered}}(r_0,r_{\mathrm{m}}) = \Phi_{\mathrm{DP}}^{\mathrm{filtered}}(r_{\mathrm{m}}) - \Phi_{\mathrm{DP}}^{\mathrm{filtered}}(r_0) \quad (2b)$$

$$I(r_0,r_m) = 0.46b\int_{r_0}^{r_m}[Z_{\mathrm{H}}^{\mathrm{M}}(r)]^b dr \quad (2c)$$

$$I(r,r_m) = 0.46b\int_{r}^{r_m}[Z_{\mathrm{H}}^{\mathrm{M}}(r)]^b dr \quad (2d)$$

$$C(r_0,r_m) = \int_{r_0}^{r_m}|\Phi_{\mathrm{DP}}^{\mathrm{rec}}(s,\alpha) - \Phi_{\mathrm{DP}}^{\mathrm{filtered}}(s)|ds \quad (2e)$$

$$\Phi_{\mathrm{DP}}^{\mathrm{rec}}(r_0,r_m) = \int_{r_0}^{r_m}\frac{A_{\mathrm{H}}(s,\alpha)}{\alpha}ds \quad (2f)$$

$$Z_{\mathrm{H}}^{\mathrm{C}}(r) = Z_{\mathrm{H}}^{\mathrm{M}}(r) + 2\int_0^r A_{\mathrm{H}}(s,\alpha)ds \quad (2g)$$

where $Z_{\mathrm{H}}^{\mathrm{M}}$ and $Z_{\mathrm{H}}^{\mathrm{C}}$ denote the measured and attenuation corrected Z_{H}, respectively; $\Phi_{\mathrm{DP}}^{\mathrm{filtered}}$ represents the Φ_{DP} profile after filtering the δ bumps from Ψ_{DP}; $\Phi_{\mathrm{DP}}^{\mathrm{rec}}$ is the reconstructed Φ_{DP} profile in the ZPHI processing chain. The optimal coefficient α is searched within the predefined range [0.03, 0.18] with a step of 0.01, through minimizing the difference between $\Phi_{\mathrm{DP}}^{\mathrm{filtered}}$ and $\Phi_{\mathrm{DP}}^{\mathrm{rec}}$ in Eq. (2e). The coefficient *b* in Eqs. (2a), (2c) and (2d) is assumed to be a constant of 0.78 on an average basis. Overall, the ZPHI method integrates $Z_{\mathrm{H}}^{\mathrm{M}}$ and the Φ_{DP} difference (Eq. 2b) between

range gate r_0 and r_m for each range segment. After A_{H} is estimated for each range gate between r_0 and r_m. $Z_{\mathrm{H}}^{\mathrm{M}}$ is corrected along the propagation path (i.e., each radial profile) by Eq. (2g).

Similarly, Eqs. (3a-e) illustrate the processing chain for Z_{DR} correction using the self-consistent criterion:

$$\hat{Z}_{\mathrm{DR}}(r) = \begin{cases} 0; & \overline{Z}_{\mathrm{H}}(r) < 20\mathrm{dBZ} \\ 0.048\overline{Z}_{\mathrm{H}}(r) - 0.774; & 20\mathrm{dBZ} \le \overline{Z}_{\mathrm{H}}(r) \le 45\mathrm{dBZ} \end{cases} \tag{3a}$$

$$\hat{Z}_{\mathrm{DR}}(r) = 0.00012 Z_{\mathrm{H}}^{\mathrm{C}}(r)^{2.5515} \tag{3b}$$

$$A_{\mathrm{DP}}(r;\beta) = \frac{\beta}{\alpha_{\mathrm{opt}}} A_{\mathrm{H}}(r;\alpha_{\mathrm{opt}}) \tag{3c}$$

$$Z_{\mathrm{DR}}^{\mathrm{C}}(r;\beta) = Z_{\mathrm{DR}}^{\mathrm{M}}(r) + 2\int_0^r A_{\mathrm{DP}}(s,\beta)ds \tag{3d}$$

$$Z_{\mathrm{DR}}^{\mathrm{C}}(r) = Z_{\mathrm{DR}}^{\mathrm{M}}(r) + 2\int_0^r A_{\mathrm{DP}}(s,\beta_{\mathrm{opt}})ds \tag{3e}$$

where $Z_{\mathrm{DR}}^{\mathrm{M}}$ and $Z_{\mathrm{DR}}^{\mathrm{C}}$ denote the measured and attenuation corrected Z_{DR}, respectively. It is assumed that Z_{DR} can be estimated from corrected Z_{H} based on the microphysical constraint derived from the DSD scattering simulations (Bringi et al., 2001). However, it should be noted that Eq. (3a) was used in Bringi et al. (2001), while Eq. (3b) is a new $Z_{\mathrm{DR}} - Z_{\mathrm{H}}$ relation derived using DSD measurements around Hangzhou, China. $\hat{Z}_{\mathrm{DR}}$ in Eqs. (3a) and (3b) represents the predicted Z_{DR} based on the corrected Z_{H} and it serves as the reference Z_{DR} to the measured Z_{DR} for the posterior approximation. In the Z_{DR} correction processing chain, A_{DP} is first estimated with the optimal coefficient β (i.e., β_{opt}) and the corresponding Z_{DR} is also estimated as illustrated in Eqs. (3c) and (3d). This processing procedure is then iteratively executed until the predefined tolerance difference threshold (i.e., 0.2dB) between $\hat{Z}_{\mathrm{DR}}^{\mathrm{C}}(r)$ and $Z_{\mathrm{DR}}^{\mathrm{C}}(r;\beta)$ is satisfied. The final correction of $Z_{\mathrm{DR}}^{\mathrm{M}}$ is reached following Eq. (3e).

2.2. Additional constraints

The conventional ZPHI method for attenuation correction is not integrated into current CPOL radar software system (see details in section 3.1) due to operational considerations. On the one hand, most of previous studies about ZPHI method are based on simulation data or polarimetric measurements from research radars (e.g., Bringi et al., 2001). The long-term operational application is relatively rare. On the other hand, more practical constraints should be imposed on the range profiles of Φ_{DP} in real applications. In this paper, four additional constraints are integrated to improve the effectiveness of ZPHI method:

(i) Non-negative constraint on A_{H} estimation. As shown in Eqs. (2a) and (2b), nonnegative $A_{\mathrm{H}}(r)$ can be derived with $\Phi_{\mathrm{DP}}^{\mathrm{filtered}}(r_m) \geq \Phi_{\mathrm{DP}}^{\mathrm{filtered}}(r_0)$. Eq. (2b) also shows that the negative/positive $\Delta\Phi_{\mathrm{DP}}(r_0, r_m)$ will lead to negative/positive $[10^{0.1b\alpha\Delta\Phi(r_0,r_m)} - 1]$ in Eq.(2a), which is directly related to negative/positive A_{H}. In rain region, Φ_{DP} should be monotonically increasing (i.e., $\Phi_{\mathrm{DP}}^{\mathrm{filtered}}(r_{\mathrm{m}}) \geq \Phi_{\mathrm{DP}}^{\mathrm{filtered}}(r_0)$). This constraint, which was not taken into account in previous studies, is critical in calculating the path integrated attenuation (PIA) in Eq. (2g). Otherwise, positive and negative A_{H} may be cancelled out along the whole propagation path. This may further introduce an underestimated PIA and $Z_{\mathrm{DR}}^{\mathrm{C}}(r)$ will then be under-corrected. This paper incorporates this constraint when partitioning the $\Phi_{\mathrm{DP}}^{\mathrm{filtered}}$ profiles into different range segments.

(ii) ρ_{HV} constraint on the partition of the Φ_{DP} profile. Range gates characterized by $\rho_{\mathrm{HV}} \geq 0.95$ were required in applying the traditional ZPHI method (Bringi et al., 2001). However, in reality, various ρ_{HV} values may exist on the propagation path. It is also noticed that ρ_{HV} reduction is always associated with δ bump and large Z_{H} measurements (Trömel et al., 2013; 2014), which

indicates that different hydrometeors such as wet hailstones or big raindrops may potentially dominate in these range gates. A_{H} will be overestimated if the range gates filled with spherical hailstones with $A_{\mathrm{H}} \approx 0$ dB·km^{-1} are considered liquid raindrops. Similar overestimation of A_{H} also applies in the scenarios when the range gates are contaminated with remaining clutters. Considering the similarity of hydrometeors within the range segment of $[r_0,\ r_m]$, this paper incorporates ρ_{HV} to further partition the Φ_{DP} profile into more subsections. In particular, the consecutive range gates with $\rho_{\mathrm{HV}} \geq 0.98$ are aggregated as one subsection and they are assumed to be pure rain. The consecutive range gates with $\rho_{\mathrm{HV}} \geq 0.85$ but $\rho_{\mathrm{HV}} < 0.98$ are assembled as another subsection, which are suspected to be filled with mixed-phase hydrometeors such as ice crystal mixed with supercooled water or melting snowflakes in the melting layer. The threshold of 0.85 is used to avoid serious contamination of non-meteorological clutters.

(iii) Convergence constraint on the cost function. No rigorous convergence checking is carried out in previous studies. Generally, the optimal α is iteratively searched through minimizing the cost function in Eq. (2e), and the computation will stop if α is determined in the predetermined range [0.03, 0.18], for range segment $[r_0,\ r_m]$. However, if $\Phi_{\mathrm{DP}}^{\mathrm{rec}}$ is larger than $\Phi_{\mathrm{DP}}^{\mathrm{filtered}}$ in $[r_0,\ r_m]$, even for the optimal α, Eq. (2e) will converge abnormally and an overestimated A_{H} is expected within this range interval. In this research, a new range gate near $(r_0 + r_m)/2$ is reselected using the split-half method for further range partitioning in order to obtain more independent α values in these new range intervals. Such constraint can avoid apparent computation convergence of Eq. (2e) due to inadequate range gate partitions since the mixed-phase hydrometeors may have similar ρ_{HV} values.

(iv) An exponential $Z_{\mathrm{DR}} - Z_{\mathrm{H}}$ relation, as shown in Eq. (3b), is derived at C-band using local

DSD measurements and this relation is adopted to replace the linear relation in Eq. (3a) for Z_{DR} correction. The linear relation in Bringi et al. (2001) is not realistic and it may underestimate Z_{DR}. In contrast, the exponential relation takes into account more microphysical information about local drop size and shape distributions. In particular, Z_{DR} increases slowly when $Z_{\mathrm{H}} < 20\,\mathrm{dBZ}$ while Z_{DR} grows exponentially when $Z_{\mathrm{H}} \geq 20$ dBZ. Z_{DR} derived from Eq. (3b) is always larger than that derived from Eq. (3a). In addition, the minimization of the differences between $\hat{Z}_{\mathrm{DR}}^{\mathrm{C}}(r)$ and $Z_{\mathrm{DR}}^{\mathrm{C}}(r;\beta)$ is executed and constrained on the whole range profile in the implementation.

Once all the optimal coefficients α_{opt} and β_{opt} are obtained within each $\Phi_{\mathrm{DP}}^{\mathrm{filtered}}$ range segments, the measured Z_{H} can be corrected along the whole Φ_{DP} range profile according to Eq. (2g). The measured Z_{DR} can be corrected following Eq. (3e). After the attenuation correction, both Z_{H} and Z_{DR} at radar polar coordinates are mapped to Cartesian grids with a grid resolution of 0.0025°× 0.0025° using the nearest neighbor method for subsequent rainfall applications.

3. C-band radar data analysis (Hangzhou, China)

As mentioned, polarimetric measurements from a C-band radar is used to demonstrate the improved ZPHI method. This radar is the first C-band dual-polarization radar for operational applications in China. It is also a prototype for large-scale dual-polarization upgrade of the operational C-band radar network. In this section, we use similar analysis procedure to the literature to report some of the first radar observations in eastern China.

3.1. System specification and data processing software

The system specifications of CPOL radar are listed in Table 1. For routine operations, the CPOL radar is configured with simultaneous horizontal and vertical polarization mode. As depicted in Figs.

1a-b, the CPOL radar is deployed in a mountainous environment with an elevation of 1512 m above mean sea level and it is not seriously affected by beam blockage issue. The elevation angles of its volume coverage pattern (VCP) have been set as 0.0°, 0.5°, 1.5°, 2.5°, 3.5°, 4.5°, 6.0°, 7.5° and 9.0° since September 2015. A full volume scan in this mode takes about six minutes. The base-level (level II) data is archived as a bz2 package, including the measured Ψ_{DP}, Z_{H}, Z_{DR}, ρ_{HV}, radial velocity and signal noise ratio, etc. Its azimuthal radial resolution is set as 0.46° at the three lowest elevation angles and 0.95° at other six higher elevation angles. The range gate resolution on all elevations is configured as 125 m. The radar systematic calibration is routinely conducted by Hangzhou Meteorological Bureau.

In addition, this paper uses a non-attenuated S-band radar for cross-validation. The S-band radar is located at Huangshan Mountain (hereafter referred to as HSM radar), about 80.25 km from the CPOL radar (see Fig. 1b). The HSM radar is operated using the standard VCP mode including nine scan elevation angles: 0.5°, 1.5°, 2.4°, 3.3°, 4.2°, 5.9°, 9.7°, 14.5° and 19.5°. The azimuthal resolution is 0.98°. Although the HSM radar beams near radial directions [165°, 169°] are blocked by the Lotus Peak of the mountains and its radial beams are all screened within [32°, 47°], the overlapping area between the HSM and CPOL radars is not affected by the blockage. Furthermore, as indicated in Fig.2, there is a large vertically overlapped area in the cross-section between the HSM and CPOL radars, which provides a great opportunity for their reflectivity comparison.

The radar operating software engineering (ROSE) system used for daily operation and maintenance of CPOL radar is manufactured by Metstar Company in Beijing, China. As shown in Fig. 3, ROSE consists of the radar data acquisition (RDA) subsystem for real-time radar signal

processing and radar product generation (RPG) system for producing timely products. Several quality control procedures, including ground clutter identification and mitigation for Z_{H}, second-trip echo identification and suppression for *V*r, and the "birdbath" scan for Z_{DR} calibration, are manually integrated into the RDA subsystem. The attenuation correction for Z_{H} and Z_{DR} has not been integrated into the RDA subsystem yet, which is expected to improve the RPG products in future.

There are eight Parsivel (Particle Size and Velocity) disdrometer units deployed around Hangzhou (see Fig. 4a), which have been collecting in situ DSD data since January 2016. The DSD measurements are the most important surface observations that can be used to derive appropriate radar rainfall relations. In this study, the temporal resolution of all the disdrometers is configured as one minute. The nearest and farthest disdrometers are 30 km and 120 km away from the CPOL radar, respectively. Except Daoshi and Shiling stations, all other six stations are national-level meteorological stations and all are supported with municipal electricity. They are well maintained to ensure the DSD data quality and the real time data series are streamed to the server machine through special wires.

In addition, 2883 tipping-bucket gauge stations (see Fig. 4b) are deployed within the range of 200 km from the CPOL radar. The temporal resolution of these surface gauge measurements is also configured as one minute. The gauge observations without any interruptions are used for verification of radar rainfall estimates. In addition, to ensure the credibility of the quantitative evaluation, the inverse distant weighting method is applied to estimate the rainfall at each gauge location with the nearest five stations: if the normalized difference between the estimated value and real gauge measurement is higher than 4, this gauge recording will be discarded in the evaluation analysis.

3.2 Z_{DR} calibration and data quality control

The "birdbath" scan is used in this study for periodic Z_{DR} calibration, which is performed in the light rain scenarios. In particular, the vertical pointing observations (elevation of 90°) through a full azimuthal rotation (Bringi and Chandrasekar, 2001) is conducted before the flood season over eastern China every year. Fig. 5 illustrates an example Z_{DR} "birdbath" scan performed at 1835 UTC, 24 April 2015, from which the melting layer can be easily identified at the altitude of 3.5-4.5km with the simultaneous increase in Z_H and Z_{DR} but decrease in ρ_{HV} (see Figs. 5a-5c). The light rain was expected below the melting layer and a Z_{DR} bias of -0.6 dB was automatically detected and sent back to the RDA subsystem to correct the systematic bias of Z_{DR}.

As the most frequently used radar measurement, Z_H is still the key parameter used for severe weather warning operations by the meteorological bureau of China. As shown in the data flow in Fig. 3, a basic quality-control procedure has been integrated into the RDA subsystem before all the measured radar moments are compressed to a bz2 package: the static ground clutters and the clutters caused by the abnormal propagation of radar beams are effectively identified and mitigated by the clutter mitigation decision (CMD) algorithm (Hubbert et al., 2009). In the CMD algorithm, the clutter phase alignment, together with the spin change, the reflectivity texture, the standard deviation of Z_{DR} and Ψ_{DP} are integrated as the input parameters of a fuzzy logic algorithm to flag the clutter contaminated gates (Gourley et al., 2007; Hubbert et al., 2009). After filtering these non-meteorological signals, radar moments are recalculated in the RDA subsystem for application and product generation.

Another important quality control component is the Ψ_{DP} processing, which includes several

steps: (i) suppressing the spike signals along the Ψ_{DP} profile through comparing the measured Ψ_{DP} at one range gate with four nearest range gates on both directions. If the difference between any range gate and the target gate is larger than 45°, Ψ_{DP} value of the target volume will be replaced with the averaged Ψ_{DP} value of these nearest range gates; (ii) unfolding Ψ_{DP} if the measurement exceeds 360° according to the standard deviation of Ψ_{DP} within nine consecutive range gates (Wang and Chandrasekar, 2009), especially in the scenarios with a large area of severe convective precipitation; (iii) FIR filtering to eliminate the δ bumps on the Ψ_{DP} range profiles (Hubbert and Bringi, 1995), and the smoothed Φ_{DP} profiles are also obtained in this step; (iv) determining the initial Φ_{DP} value along each range profile and then removing it from the whole Φ_{DP} range profile. With these preprocessing steps, zero-started and smoothed Φ_{DP} range profiles can be formed for further ZPHI processing.

In order to mitigate the large fluctuations of ρ_{HV}, this paper simply smooths the ρ_{HV} measurements using the nearest five radial range gates. The zero-started Φ_{DP} profile (i.e., $\Phi_{DP}^{filtered}$), clutter-filtered Z_H^M and smoothed ρ_{HV} are integrated as inputs to the improved attenuation correction approach presented in section 2.1, with additional constraints described in section 2.2.

3.3 Precipitation events

Two severe convective precipitation events during Meiyu season are utilized to demonstrate the performance of the improved ZPHI method. Meiyu Front is one of the most important weather phenomena that affects eastern China. It is always coupled with considerable water-vapor transferring from the Bay of Bengal when the subtropical high pressure gradually moves to the north of China in

June. Meiyu Front frequently passes over the mountainous area across Anhui, Jiangxi and Zhejiang provinces and severe weather disasters occur nearly every year.

The CPOL radar effectively observed these two precipitation events as depicted in Fig. 6, though the radar signals were attenuated by the severe convective rainstorms. One precipitation event was a severe convective weather event during 2000 UTC, 31 May 2016 and 0800 UTC, 01 June 2016 with the rainstorms passing over the CPOL radar from the northwest to southwest. During this event, the maximum gauge 2-h rainfall accumulations at Qiandao Lake Country reached 121.2 mm at 0500 UTC, 01 June 2016, and Jiande Town of Hangzhou suffered from serious water-logging on this day. As shown in Fig. 6a, the azimuthal directions within [20°, 35°], [85°, 87°] and [280°, 284°] all exhibit rapid Ψ_{DP} increasing and the maximum zero-started Ψ_{DP} values in [280°, 284°] are over 400°. The other case was an extreme event occurred during 1800 UTC, 23 June 2017 and 0200 UTC, 24 June 2017. The convective rainstorms embedded in the mesocyclone system slowly passed over the cross borders of Anhui, Zhejiang and Jiangxi provinces. The northwestern of Quzhou city suffered from a serious debris flow during this event and the maximum 3-h rainfall accumulation recorded by gauges near this area reached 141.9 mm at 0300 UTC, 24 June 2017. Similar to the former event, zero-started Ψ_{DP} data at 0001 UTC, 24 June 2017 shows that the maximum Ψ_{DP} in the azimuthal directions of [203°, 216°] were over 300° (see Fig. 6b).

Although large areas with high Z_H and Z_{DR} values are presented in the measured fields in Figs. 6c~6f, the attenuation on Z_H and Z_{DR} are both evident along the azimuthal directions with dramatic increase of zero-started Ψ_{DP}. For example, Z_H and Z_{DR} in the azimuthal directions within [20°, 35°] on Figs. 6c and 6e, and [203°, 216°] in Figs. 6d and 6f suffer from serious attenuation, which makes

both Z_{H} and Z_{DR} featured with typical "V-notch" shape along these two azimuthal direction intervals (mainly caused by severe rainstorms). Z_{H} and Z_{DR} in the azimuthal directions of [85°, 87°] and [280°, 284°] in Figs. 6c and 6e also suffered serious attenuation, which introduces significant signal loss according to the post analysis. In addition, a large area of Z_{DR} in Figs. 6e and 6f was attenuated to below -6.5dB far behind these two rainstorm areas. Such attenuation effects significantly degraded the performance of radar QPE derived from $R(Z_{\mathrm{H}})$ or $R(Z_{\mathrm{H}}, Z_{\mathrm{DR}})$. Using these attenuated measurements to decide the severity order of the timely weather warning could be misleading.

3.4. Attenuation correction performance

In order to evaluate the performance of the proposed attenuation correction scheme, this paper also utilizes the aligned S-band observations to verify the CPOL radar measurements before and after attenuation correction. Qualitative analysis using DSD dataset collected near the CPOL radar is also conducted to further demonstrate the feasibility and practical effectiveness of this improved attenuation correction approach. For illustration purposes, sample CPOL radar measurements at 0° elevation angle before/after attenuation correction during the two extreme events are respectively illustrated in Figs. 6 and 7, and the collocated S-band observations from HSM radar are indicated in in Figs. 7e and 7f. The Z_{H} comparison in the cross-section area between the CPOL and HSM radar is also illustrated in Fig. 8.

3.4.1 Comparison of CPOL radar with HSM radar

Compared with the measured $Z_{\mathrm{H}}^{\mathrm{M}}$ and $Z_{\mathrm{DR}}^{\mathrm{M}}$ in Figs. 6c-6f, attenuation corrected $Z_{\mathrm{H}}^{\mathrm{C}}$ and $Z_{\mathrm{DR}}^{\mathrm{C}}$ in Figs. 7c-f are significantly enhanced, although the Z_{H} measurement in Fig. 7c still suffers from some signal loss behind the convective regions compared with the HSM radar observations (see Fig.

7g). $Z_{\mathrm{H}}^{\mathrm{C}}$ and $Z_{\mathrm{DR}}^{\mathrm{C}}$ in the convective rainstorms are accompanied with large K_{DP} values ($K_{\mathrm{DP}} > 0.5$ deg·km^{-1} in Figs. 7a and 7b) and they agree well with the Z_{H} observed by HSM radar (see Figs. 7g and 7h). Here, it should be noted that the wet radome effect on Z_{H} measurements in Figs. 7c and 7e can be neglected since only light rain is observed at the CPOL radar station. However, the wet radome effect cannot be ignored in Figs. 7d and 7f, where moderate rain is presented in Figs. 7d and 7f. The remaining differences between S-band and attenuation corrected C-band observations can be attributed to the differences in volume resolution, measurement time, and beam broadening of the two radar systems.

Figs. 8a-8c further illustrate the reflectivity measurements in the common cross-section area between the CPOL and HSM radar at 0000 UTC, 01 June 2016. The convective storm cell 2 near CPOL radar (but far from HSM radar) in Fig. 8b is characterized with larger Z_{H} than storm cell 1, which is far from CPOL radar. This is different from what is observed by the S-band HSM radar (see Fig. 8a). However, the attenuation corrected fields in storm cells 1 and 2 in Fig. 8c are more consistent with the collocated S-band measurements in Fig. 8a, which actually shows that the storm cell 1 has higher Z_{H} than cell 2. Such comparison results qualitatively verify the effectiveness of the proposed attenuation correction procedure.

Figs. 8d and 8e show the scatter density plots of Z_{H} from the CPOL radar versus HSM radar within their common range volumes. The scatter number within [10 dBZ, 35 dBZ] in Fig. 8e is smaller than that in Fig. 8d along the diagonal line (1:1) since part of the measured $Z_{\mathrm{H}}^{\mathrm{M}}$ from CPOL radar has been corrected to higher Z_{H} values. In consequence, the scatter density within [35dBZ, 50dBZ] is significantly increased in Fig. 8e, which means $Z_{\mathrm{H}}^{\mathrm{C}}$ of CPOL radar is more consistent with Z_{H}

from HSM radar. Although signal loss and/or the differences in range resolution can account for the sparse points in Figs. 8d-8e, the measured $Z_{\mathrm{H}}^{\mathrm{M}}$ from CPOL radar can be effectively enhanced by the proposed attenuation correction approach. A more quantitative verification of the attenuation correction performance can be achieved through the following statistical score:

$$\Delta Z_{\mathrm{H}} = \frac{1}{n}(Z_{\mathrm{HS}} - Z_{\mathrm{HC}}) \tag{4}$$

where Z_{HS} represents reflectivity from the S-band HSM radar; Z_{HC} represents the CPOL radar reflectivity; n is the total number of common resolution volumes as depicted in Fig. 2. Again, it should be noted that the range resolution of HSM radar is eight times bigger than CPOL radar, so one range gate of HSM radar may correspond to eight range gates of CPOL radar in Eq. (4). ΔZ in Fig. 8d is 2.26 dBZ, whereas it is 0.69 dBZ for Fig. 8e. This, again, demonstrates the effectiveness of the improved ZPHI method.

3.4.2 Comparison with DSD simulations

Comparison with polarimetric radar moments simulated based on DSD data is another efficient way to verify the attenuation correction performance. In this paper, the DSD measurements from eight Parsivel units during June 2016 and 2017 are utilized in the comparison study. In total, this DSD dataset contains 70680 valid measurements after eliminating 69 measurements that are possibly contaminated by hail (featured with large Z_{H} but near-zero Z_{DR}). Z_{H}, Z_{DR}, and K_{DP} at C-band frequency are simulated using *T*-matrix method, assuming the raindrop aspect ratio in Brandes et al. (2002) at temperature of 20℃. Rainfall rate (R) is also computed directly from the DSD dataset. Scattergrams of the simulated Z_{DR} versus Z_{H}, K_{DP} versus Z_{H}, and $K_{\mathrm{DP}}/Z_{\mathrm{Hl}}$ (Z_{H} in the linear scale) versus Z_{DR} are illustrated in Figs. 9a-9c. Similarly, Figs. 10 and 11 show the scatter density

distributions of CPOL radar Plan Position Indicator (PPI) observations illustrated in Figs. 6 and 7. The black dots overlaid on the color density plots in Figs. 10 and 11 stand for the simulated radar moments based on the DSD data. It is concluded that:

(i) A large amount of Z_{DR} measurements are attenuated to negative values with the minimum Z_{DR} decreased below -4dB in Figs. 10a and 11a (i.e., before attenuation correction). Without attenuation correction, this phenomenon seriously violates the theoretical fact that Z_{DR} grows exponentially as Z_{H} increases. As a result, the scatter distributions of Z_{H} and Z_{DR} in both Figs. 10a and 11a are inconsistent with those in Fig. 9a, particularly in the Z_{H} interval of [10 dBZ, 40 dBZ], which corresponds to the light to moderate rainfall. This is because most parts of Z_{H} and Z_{DR} measurements are severely attenuated when radar beam passing through the rainstorm. On the contrary, Z_{H} and Z_{DR} distributions in Figs. 10b and 11b are much more consistent with the simulated data in Fig. 9a. Many negative Z_{DR} measurements are corrected to positive values in the Z_{H} interval of [10 dBZ, 40 dBZ]. Scattergrams of Z_{DR} versus Z_{H} in Figs. 10b and 11b are also enhanced when Z_{H} exceeds 40 dBZ, which demonstrates the capability of the proposed attenuation correction method to resolve the serious attenuation introduced by severe convective rainstorms.

(ii) The specific differential phase K_{DP}, which is immune to attenuation, is also used as an objective reference to show the effectiveness of Z_{H} correction. Larger K_{DP} value is directly related to higher liquid water content if only liquid hydrometeors are contained in one range volume. Scattergram of K_{DP} versus Z_{H} after attenuation correction (see Figs. 10d and 11d) is more realistic and consistent with Fig. 9b than that before attenuation correction (see Figs. 10c and 11c). In particular, higher scatter density is presented with increasing Z_{H} and K_{DP} after correction and more

scatter pixels concentrate near Z_{H} interval of 40-50dBZ with K_{DP} larger than 0.5deg·km^{-1} in Figs. 10d and 11d than that in Figs. 10c and 11c, which implies that $Z_{\mathrm{H}}^{\mathrm{C}}$ and K_{DP} values are particularly consistent in the heavy rain regions after correction.

(iii) Similarly, the scattergrams of $K_{\mathrm{DP}}/Z_{\mathrm{Hl}}$ versus Z_{DR} are shown in Figs. 10e-f and 11e-f. Such distribution is often used to identify different precipitation regimes (i.e., convective or stratiform). It is observed that many scatter pixels are distributed in the Z_{DR} interval of -4-0dB in Figs. 10e and 11e due to the attenuation. The attenuated data also makes the scatter density center deviate seriously from the simulated data in Fig. 9c. The distributions in Figs. 10f and 11f concentrate more around the center at ($Z_{\mathrm{DR}} = 0$ dB, $K_{\mathrm{DP}}/Z_{\mathrm{Hl}} = 10^{-4}$ deg·km^{-1}·mm^{-6}·m^{3}) with much fewer negative Z_{DR} values and they look more consistent with the simulation data in Fig. 9c. In addition, many measured negative Z_{DR} values in Figs. 10e and 11e have been corrected to positive values in Figs. 10f and 11f. Nevertheless, there are still some negative Z_{DR} values in Figs. 10 and 11 after attenuation correction; the former case in Fig. 10f may be caused by some non-spherical hydrometeors such as ice crystals and melting snowflakes, whereas the latter case in Fig. 11 is likely affected by the wet radome effect which can be inferred from Z_{H} and Z_{DR} plots in Figs. 6 and 7 (Bechini et al., 2006; Gorgucci et al., 2013).

4. Impact on radar QPE

4.1 Radar rainfall algorithms

Utilizing the DSD observations around Hangzhou during June of 2016 and 2017, the local radar rainfall rate relationships based on Z_{H}, Z_{DR} and K_{DP} are obtained for CPOL radar based on the standard weighted least squares nonlinear fitting method. In particular, one $R(Z_{\mathrm{H}}, Z_{\mathrm{DR}})$, two $R(Z_{\mathrm{H}})$

and two $R(K_{\mathrm{DP}})$ relations are derived with respect to the DSD density distribution and thresholds on polarimetric variables.

$$R(Z_{\mathrm{H}}, Z_{\mathrm{DR}}) = 0.0109 \times Z_{\mathrm{H}}^{0.8365} Z_{\mathrm{DR}}^{-1.87} \quad (5a)$$

$$R(Z_{\mathrm{H}}) = 0.0496 \times Z_{\mathrm{H}}^{0.6153} \qquad Z_{\mathrm{H}} < 40\mathrm{dBZ} \quad (5b)$$

$$R(Z_{\mathrm{H}}) = 0.0496 \times Z_{\mathrm{H}}^{0.6153} \qquad Z_{\mathrm{H}} \geq 40\mathrm{dBZ} \quad (5c)$$

$$R(K_{\mathrm{DP}}) = 25.7689 \times K_{\mathrm{DP}}^{0.7782} \qquad K_{\mathrm{DP}} < 0.5\mathrm{deg} \cdot \mathrm{km}^{-1} \quad (5d)$$

$$R(K_{\mathrm{DP}}) = 32.7928 \times K_{\mathrm{DP}}^{0.7782} \qquad K_{\mathrm{DP}} \geq 0.5\mathrm{deg} \cdot \mathrm{km}^{-1} \quad (5e)$$

where Z_{H} and Z_{DR} are in linear scale. For $R(Z_{\mathrm{H}})$ estimators, as depicted in Figs. 9d and 9e, the relationship in Eq. (5b) mainly represents light to moderate rain, whereas Eqs (5c) mainly represents the heavy rain region. Similarly, the $R(K_{\mathrm{DP}})$ estimators in Eqs. (5d) and (5e) respectively represent light to moderate rain and heavy rain. The thresholds are predefined according to the scatter plots in Fig.9. It can be seen in Fig. 9b that Z_{H}<40dBZ coexists with $K_{\mathrm{DP}} < 0.5$ deg·km^{-1}, while Z_{H} becomes larger than 40 dBZ when K_{DP} increases.

These three radar QPE estimators are tested independently using the CPOL radar measurements during the two precipitation events described in section 3.3. The normalized mean absolute error (E_{NMA}), root mean square error (E_{RMS}), and correlation coefficient (E_{CC}) are calculated for each radar-derived hourly rainfall accumulation.

$$E_{\mathrm{NMA}} = \frac{\sum_{i=1}^{n} |r_i - g_i|}{\sum_{i=1}^{n} g_i} \quad (6a)$$

$$E_{\mathrm{RMS}} = \sqrt{\frac{1}{n} \sum_{i}^{n} |r_i - g_i|^2} \quad (6b)$$

$$E_{\mathrm{CC}} = \frac{\sum_{i=1}^{n} (r_i - \overline{r})(g_i - \overline{g})}{\sqrt{\sum_{i=1}^{n} (r_i - \overline{r})^2} \sqrt{\sum_{i=1}^{n} (g_i - \overline{g})^2}} \quad (6c)$$

where r_i and g_i are hourly rainfall accumulations from radar and gauge, respectively; $\overline{r}$ and $\overline{g}$ stand for the sample averages of all radar and gauge pairs within the coverage range of CPOL radar.

4.2 Quantitative evaluation of hourly rainfall products

Radar-derived QPE serves as another effective way to verify the performance of the improved attenuation correction approach. Hereafter, radar QPE estimators based on the measured Z_{H} and Z_{DR} are denoted as $R(Z_{\mathrm{H}}^{\mathrm{M}})$ and $R(Z_{\mathrm{H}}^{\mathrm{M}}, Z_{\mathrm{DR}}^{\mathrm{M}})$, and those based on the corrected fields are denoted as $R(Z_{\mathrm{H}}^{\mathrm{C}})$ and $R(Z_{\mathrm{H}}^{\mathrm{C}}, Z_{\mathrm{DR}}^{\mathrm{C}})$. These two radar QPE estimators are first used to verify the effectiveness of the improved ZPHI method at different range distances and the performance is compared with conventional ZPHI method. In particular, radar radial range of 200 km is partitioned into four evenly spaced segments (see Fig. 4b). There are 182, 604, 992 and 1105 surface weather stations within the range [0, 50km), [50km, 100km), [100km, 150km) and [150km,200km], respectively. E_{NMA}, E_{RMS} and E_{CC} are calculated for each range interval. The scattergrams of rainfall estimates and quantitative scores are shown in Figs. 11-14 and Table 2. The analysis is performed from the following aspects:

(i) Comparison of $R(Z_{\mathrm{H}}^{\mathrm{C}})$ versus $R(Z_{\mathrm{H}}^{\mathrm{M}})$, and $R(Z_{\mathrm{H}}^{\mathrm{C}}, Z_{\mathrm{DR}}^{\mathrm{C}})$ versus $R(Z_{\mathrm{H}}^{\mathrm{M}}, Z_{\mathrm{DR}}^{\mathrm{M}})$.

In the improved ZPHI approach, Eq. (2g) for Z_{H} correction along the radial range profile can be rewritten as

$$Z_{\mathrm{H}}^{\mathrm{C}}(r) = Z_{\mathrm{H}}^{\mathrm{M}}(r) + \mathrm{PIA}(r_0) + 2\int_{r_0}^{r} A_{\mathrm{H}}\big(s, \alpha_{\mathrm{opt}}\big)ds \tag{7a}$$

$$\mathrm{PIA}(r_0) = 2\int_{0}^{r_0} A_{\mathrm{H}}(s)ds \tag{7b}$$

where $r_0 \le r \le r_m$. Eq. (7b) refers to the PIA before $r_0$and it may involve several independent α coefficients, which are likely different from those in $[r_0, r_m]$. $Z_{\mathrm{H}}^{\mathrm{M}}(r)$ at longer distances can be enhanced by PIA in $[0, r_0]$ and PIA in $[r_0, r]$, because $A_{\mathrm{H}}(r)$ at each range gate is constrained as positive and PIA is monotonically increasing with range. As a result, most scatter pixels are above the diagonal line in Figs. 12a-12d. Because the same *Z*-*R* relationships are applied, this phenomenon can be attributed to the enhanced Z_{H} measurements due to attenuation correction.

However, only scatter distribution trend in Figs. 12e and 12f is similar to that in Figs. 12a-d.

Compared with $R(Z_{\mathrm{H}}^{\mathrm{M}}, Z_{\mathrm{DR}}^{\mathrm{M}})$, the enhancement introduced by $R(Z_{\mathrm{H}}^{\mathrm{C}}, Z_{\mathrm{DR}}^{\mathrm{C}})$ is gradually weakening and rainfall estimates derived from $R(Z_{\mathrm{H}}^{\mathrm{M}}, Z_{\mathrm{DR}}^{\mathrm{M}})$ and $R(Z_{\mathrm{H}}^{\mathrm{C}}, Z_{\mathrm{DR}}^{\mathrm{C}})$ are comparable in Figs. 12f and 12h. This can be explained by the intrinsic characteristics of Eq. (5a). That is, the Z_{H}-related part shows obvious monotonically increasing trend in Fig. 15a, but the Z_{DR}-related part shows monotonically decreasing trend in Fig. 15b since the exponent of the latter part is negative. Although Z_{H} and Z_{DR} can be attenuated simultaneously, Z_{H}- and Z_{DR}-related parts may compromise with each other for rainfall applications. After attenuation correction, both $Z_{\mathrm{H}}$and Z_{DR} are enhanced, but the increasing Z_{H}-related part and the decreasing Z_{DR}-related part will again compromise with each other.

(ii) Comparison of $R(Z_{\mathrm{H}})$ and $R(Z_{\mathrm{H}}, Z_{\mathrm{DR}})$ with hourly rainfall observed by gauges.

Figs. 13a and 14a show that $R(Z_{\mathrm{H}}^{\mathrm{M}})$ and $R(Z_{\mathrm{H}}^{\mathrm{M}}, Z_{\mathrm{DR}}^{\mathrm{M}})$ seriously underestimate rainfall in the range interval of [0km, 50km) and their E_{NMA} scores at all range intervals are negative. In addition, E_{NMA}, E_{RMS} and E_{CC} scores of $R(Z_{\mathrm{H}}^{\mathrm{M}})$ and $R(Z_{\mathrm{H}}^{\mathrm{M}}, Z_{\mathrm{DR}}^{\mathrm{M}})$ present similar decreasing trends in Table 2 as the distance increases. Although E_{RMS} is apparently decreasing with the increasing distance, E_{CC} scores are not, mainly due to the coexistence of overestimation and underestimation as inferred by Figs. 13b-d and Figs. 14b-d.

On the other hand, $R(Z_{\mathrm{H}}^{\mathrm{C}})/R(Z_{\mathrm{H}}^{\mathrm{C}}, Z_{\mathrm{DR}}^{\mathrm{C}})$ performs much better than $R(Z_{\mathrm{H}}^{\mathrm{M}})/R(Z_{\mathrm{H}}^{\mathrm{M}}, Z_{\mathrm{DR}}^{\mathrm{M}})$ according to Table 2. E_{RMS} and E_{CC} scores of $R(Z_{\mathrm{H}}^{\mathrm{C}})/R(Z_{\mathrm{H}}^{\mathrm{C}}, Z_{\mathrm{DR}}^{\mathrm{C}})$ are all superior to those of $R(Z_{\mathrm{H}}^{\mathrm{M}})/R(Z_{\mathrm{H}}^{\mathrm{M}}, Z_{\mathrm{DR}}^{\mathrm{M}})$ at all range intervals. This improvement can be attributed to the improved performance of attenuation correction so that the underestimation of $R(Z_{\mathrm{H}}^{\mathrm{M}})/R(Z_{\mathrm{H}}^{\mathrm{M}}, Z_{\mathrm{DR}}^{\mathrm{M}})$ in Figs. 13e-h and Figs. 14e-h can be effectively mitigated.

E_{NMA} scores of $R(Z_{\mathrm{H}}^{\mathrm{C}})$ are all positive in Table 2, which implies that $R(Z_{\mathrm{H}}^{\mathrm{C}})$ is overestimating rainfall. This is also illustrated by Figs. 13g and h. Such overestimation is likely caused by the fact that radar measurements above the ground are not always consistent with the surface measurements: radar inherently samples hydrometeors in the air but gauge observes rainfall accumulations near the

surface. Furthermore, hydrometeors may be intrinsically evolving during their falling process, especially in the thunderstorm and hailstorm scenarios. When severe convective rainstorms pass over an area, Z_{H} often presents with large measurements in the air, but surface rain gauge recordings may be delayed due to the convective updraft lifting and subsequent overestimation of radar QPE is expected, which may account for the overestimated scatters in Figs. 13g and 13h.

(iii) The uncertainties of conventional ZPHI method.

All the four additional constraints described in section 2.2 aim to mitigate the underestimation or overestimation of A_{H} by conventional ZPHI method. If no constraint is imposed, negative A_{H} may be derived and it will compromise with positive A_{H}, which will result in miscorrection of $Z_{\mathrm{H}}^{\mathrm{C}}$ and $Z_{\mathrm{DR}}^{\mathrm{C}}$. For example, the contamination of hailstones and/or clutters on the filtered Φ_{DP} profile, or the abnormal convergence of the cost function will cause overestimation of A_{H} and subsequent $Z_{\mathrm{H}}^{\mathrm{C}}$ and $Z_{\mathrm{DR}}^{\mathrm{C}}$. The linear $Z_{\mathrm{DR}} - Z_{\mathrm{H}}$ relations may also lead to miscalculation of Z_{DR}. As aforementioned, $R(Z_{\mathrm{H}}^{\mathrm{C}})$ may overestimate rainfall at longer distances even after attenuation correction using the improved ZPHI method. In conventional ZPHI method, the overestimation/underestimation of A_{H} may further deteriorate the performance of $R(Z_{\mathrm{H}}^{\mathrm{C}})$ at longer distances due to the PIA effects. The uncertainties of $R(Z_{\mathrm{H}}^{\mathrm{C}}, Z_{\mathrm{DR}}^{\mathrm{C}})$ will be further deteriorated as well, due to the compromise between Z_{H}- and Z_{DR}-related part in Eq. (5a), though the performance scores of $R(Z_{\mathrm{H}}^{\mathrm{C}}, Z_{\mathrm{DR}}^{\mathrm{C}})$ may not be degraded apparently.

(iv) Comparison of $R(Z_{\mathrm{H}})$ and $R(Z_{\mathrm{H}}, Z_{\mathrm{DR}})$ with $R(K_{\mathrm{DP}})$.

Hourly rainfall accumulations based on $R(K_{\mathrm{DP}})$ are calculated for cross-validation purposes. The E_{NMA}, E_{RMS} and E_{CC} scores of $R(Z_{\mathrm{H}})$, $R(Z_{\mathrm{H}}, Z_{\mathrm{DR}})$ and $R(K_{\mathrm{DP}})$ within the coverage range of 100km (less beam broadening effect) are listed in Table 3. The scatter density plots of various radar-derived products are illustrated in Fig. 16. It is concluded that the hourly rainfall estimates derived from $R(K_{\mathrm{DP}})$ perform the best among all radar QPE estimators and they agree very well with gauge

observations (see Fig. 16a). As such, we use $R(K_{\mathrm{DP}})$ as a reference to verify the improvement of $R(Z_{\mathrm{H}})$ and $R(Z_{\mathrm{H}}, Z_{\mathrm{DR}})$. Figs. 16b and c show that $R(Z_{\mathrm{H}}^{\mathrm{M}})$ and $R(Z_{\mathrm{H}}^{\mathrm{M}}, Z_{\mathrm{DR}}^{\mathrm{M}})$ produce less rainfall than $R(K_{\mathrm{DP}})$ because of the attenuation. In contrast, $R(Z_{\mathrm{H}}^{\mathrm{C}})$ and $R(Z_{\mathrm{H}}^{\mathrm{C}}, Z_{\mathrm{DR}}^{\mathrm{C}})$ can provide comparable estimates with $R(K_{\mathrm{DP}})$, as shown in Figs. 16e and 16f. The estimates from $R(Z_{\mathrm{DR}}^{\mathrm{C}})$ and $R(Z_{\mathrm{H}}^{\mathrm{C}}, Z_{\mathrm{DR}}^{\mathrm{C}})$ agree well with each other too (see Fig. 16d). These comparison results further indicate that the attenuations on Z_{H} and Z_{DR} are effectively compensated using the improved correction approach in this paper. Comparable radar QPE performance can be achieved using $R(Z_{\mathrm{H}})$ and $R(Z_{\mathrm{H}}, Z_{\mathrm{DR}})$ with relative to $R(K_{\mathrm{DP}})$, which is essentially attributed to the enhanced self-consistency between $Z_{\mathrm{H}}^{\mathrm{C}}$, $Z_{\mathrm{DR}}^{\mathrm{C}}$ and K_{DP}.

4.3 Discussion

The attenuation due to propagation in rain is an important error source in high-frequency radar (e.g., C- and X-band) QPE applications. In this paper, four additional constraints are imposed to the ZPHI approach for improved correction of Z_{H} and Z_{DR} in practical environment. Radar QPE performance is significantly improved after attenuation correction. The attenuation corrected Z_{H} and Z_{DR} are also useful for other applications such as DSD retrievals and cloud microphysical research. However, additional issues should be considered for future applications. First, partial beam blockage in Z_{H} measurements cannot be neglected in complex terrain especially when this issue is mixed with attenuation in rain, which will make Z_{H} in Eq. (2a) even smaller than expected. In such scenarios, A_{H} will be underestimated, and Z_{H} will then be under-corrected, resulting an underestimation of rainfall from $R(Z_{\mathrm{H}})$. The system calibration of Z_{H} and Z_{DR} should also be taken into account. Positive/negative bias of Z_{H} will cause underestimation/overestimation of A_{H}. Since the ZPHI

method starts from Eq. (2a), reliable Z_{H} and Z_{DR} measurements are indispensable for practical implementations. This will require periodic check on the system biases. Also, in moderate to heavy rain conditions, the wet radome effect cannot be neglected. More uncertainties are expected if these negative effects coexist at the same time. The characteristics of K_{DP}, as well as the self-consistency between Z_{H}, Z_{DR} and K_{DP}, are very promising in such cases. But the estimation of K_{DP} is not a trivial task, and the Ψ_{DP} measurement along the propagation path may be very noisy with large fluctuation especially in light rain. Comprehensive utilization of Z_{H}, Z_{DR} and K_{DP} could possibly provide a better solution to radar QPE (e.g., Chen et al., 2017a). Furthermore, radar rainfall relationships should be designed adaptively in order to capture the temporal evolving characteristics of rainstorms (Gou et al., 2018).

5. Summary

This paper proposes an improved ZPHI method with four additional constraints on the attenuation correction of Z_{H} and Z_{DR}. This new method is evaluated using two extreme precipitation events by comparing with non-attenuated S-band observations, simulated radar variables from DSD dataset, and hourly rainfall measurements from gauges. Three radar-derived rainfall estimators, namely, $R(Z_{\mathrm{H}})$, $R(Z_{\mathrm{H}}, Z_{\mathrm{DR}})$ and $R(K_{\mathrm{DP}})$, are implemented to further demonstrate the attenuation correction performance and its impact on radar QPE. The main results are summarized as follows: Both the qualitative and quantitative evaluation results show that the proposed attenuation correction procedure can effectively enhance the measured Z_{H} and Z_{DR}. The attenuation corrected data are more consistent with collocated S-band observations. The self-consistency between K_{DP}, Z_{H} and Z_{DR} is greatly improved after attenuation correction and they

show better agreement with the simulated radar moments derived from real DSD data collected around Hangzhou area. The performance of $R(Z_{\mathrm{H}})$ and $R(Z_{\mathrm{H}}, Z_{\mathrm{DR}})$ is significantly improved after attenuation correction. In particular, all the evaluation scores of radar-derived hourly rainfall product are superior to those before attenuation correction. Both $R(Z_{\mathrm{H}})$ and $R(Z_{\mathrm{H}}, Z_{\mathrm{DR}})$ based on corrected Z_{H} and Z_{DR}can produce comparable products to $R(K_{\mathrm{DP}})$ within the coverage range of 100 km.

All these results have demonstrated the effectiveness of the improved ZPHI method for practical applications. However, it should be noted that partial beam blockage, miscalibration and wet radome effect on Z_{H} and Z_{DR} are not taken into account in this study. In addition, the signal loss due to the large area of severe convective storms is another important issue that may hinder the correction processing. Such signal extinction is common in the summer monsoon seasons in China, future work will focus on these aspects to enhance the capability of CPOL radar for severe weather warning and nowcasting operations.

Acknowledgements: This research is primarily supported by the National Natural Science Foundation of China (NSFC) under Grants 41705018, 41705008 and 41575036, Zhejiang Provincial Natural Science Fund through award LY17D050005, and Zhejiang Major Science and Technology Special Projects through award 2017C03035. The CPOL radar, DSD and rain gauge data are provided by Hangzhou Meteorological Administration and the HSM radar is operated and managed by Anhui Meteorological Administration. The authors greatly appreciate the anonymous reviewers who helped to improve this manuscript.

References

Bechini, R., Cremonini, R., Gorgucci, E., Baldini, L., 2006. Dual-pol radar calibration and correction of the bias introduced by non uniform radome wetting. Proc. Fourth European Conf. on Radar in Meteorology, Barcelona, Spain, ERAD, 593–596.

Brandes, E.A., Zhang, G., Vivekanandan, J., 2002. Experiments in rainfall estimation with a polarimetric radar in a subtropical environment. J. Appl. Meteor. 41, 674–685.

Bringi, V.N.; Chandrasekar, V., 2001. Polarimetric Doppler Weather Radar: Principles and Applications. Cambridge University Press, 636 pp.

Bringi, V.N., Keenan, T. D., Chandrasekar, V., 2001. Correcting C-band radar reflectivity and differential reflectivity data for rain attenuation: A self-consistent method with constraints. IEEE Trans. Geosci. Remote Sens. 39, 1906-1915.

Chandrasekar, V., Wang, Y., Chen, H., 2012. The CASA quantitative precipitation estimation system: a five year validation study, Nat. Hazards Earth Syst. Sci. 12, 2811-2820.

Chandrasekar, V., Chen, H., Philips, B., 2018. Principles of high-resolution radar network for hazard mitigation and disaster management in an urban environment. Journal of the Meteorological Society of Japan. 96A, 119-139.

Chandrasekar, V., Kernen, R., Lim, S., Moisseev, D., 2013. Recent advances in classification of observations from dual-polarization weather radars. Atmos. Res. 119, 97–111.

Chen, H., Chandrasekar, V., 2018. Real-time wind velocity retrieval in the precipitation system using high-resolution operational multi-radar network. Remote Sensing of Aerosols, Clouds, and Precipitation. Elsevier, The Netherlands, 315-339.

Chen, H., Chandrasekar, V., Bechini, R., 2017a. An improved dual-polarization radar rainfall algorithm (DROPS2.0): application in NASA IFloodS field campaign. J. Hydrometeorol. 18, 917–937.

Chen, H., Lim, S., Chandrasekar, V., Jang, B.-J., 2017b. Urban hydrological applications of dual-polarization X-band radar: Case study in Korea. J. Hydrol. Eng. 22(5), E5016001.

Cifelli, R., Chandrasekar, V., Chen, H., Johnson, L. E., 2018. High resolution radar quantitative precipitation estimation in the San Francisco Bay Area: Rainfall monitoring for the urban environment. Journal of the Meteorological Society of Japan. 96A, 141-155.

Gorgucci, E., Baldini, L., 2015. Influence of beam broadening on the accuracy of radar polarimetric rainfall estimation. J. Hydrometeor. 16, 1356–1371.

Gorgucci, E., Bechini, R., Baldini, L., Cremonini, R., Chandrasekar, V., 2013. The influence of antenna radome on weather radar calibration and its real-time assessment. J. Atmos. Oceanic Technol. 30, 676–689.

Gorgucci, E., Chandrasekar, V., 2005. Evaluation of attenuation correction methodology for dual-polarization radars: Application to X-band systems. J. Atmos. Oceanic Technol. 22, 1195–1206.

Gorgucci, E., Chandrasekar, V., Baldini, L., 2006. Correction of X-band radar observation for propagation effects based on the self-consistency principle. J. Atmos. Oceanic Technol. 23, 1668–1681.

Gorgucci, E., Scarchilli, G., Chandrasekar, V., Bringi, V.N., 2000. Measurement of mean raindrop shape from polarimetric radar observations. J. Atmos. Sci. 57, 3406–3413.

Gou, Y., Ma, Y., Chen, H., Wen, Y., 2018. Radar-derived quantitative precipitation estimation in complex terrain over the eastern Tibetan Plateau. Atmospheric Research. 203, 286-297.

Gou, Y., Ma, Y., Chen, H., Yin, J., 2019. Utilization of a C-band polarimetric radar for severe rainfall event analysis in complex terrain over eastern china. Remote Sens. 11, 22.

Gourley, J., Tabary, P., du Chatelet, J. P., 2007. A fuzzy logic algorithm for the separation of precipitating from nonprecipitating echoes using polarimetric radar observations. J. Atmos. Oceanic Technol. 24, 1439–1451.

Hubbert, J., Bringi, V. N., Chandrasekar, V., 1993. Processing and interpretation of coherent dual-polarized radar measurements. J. Atmos. Oceanic Technol. 10, 155–164.

Hubbert, J., Bringi, V. N., 1995. An iterative filtering technique for the analysis of copolar differential phase and dualfrequency radar measurements. J. Atmos. Oceanic Technol. 12, 643–648.

Hubbert, J., Dixon, M., Ellis, S., 2009. Weather radar ground clutter. Part II: real-time identification and filtering. J. Atmos. Oceanic Technol. 26, 1181–1197.

Islam, T., Rico-Ramirez, M. A., Han, D., Srivastava, P. K., 2014. Sensitivity associated with bright band/melting layer location on radar reflectivity correction for attenuation at C-band using

differential propagation phase measurements, Atmospheric Research. 135-136, 143-158.

Kim, D.-S., Maki, M., Lee, D.-I., 2008. Correction of X-band radar reflectivity and differential reflectivity for rain attenuation using differential phase, Atmospheric Research. 90(1), 1-9.

Lim, S., Chandrasekar, V., 2006. A dual-polarization rain profiling algorithm. IEEE Trans. Geosci. Remote Sens. 44, 1011–1021.

Lim, S., Chandrasekar, V., 2016. A robust attenuation correction system for reflectivity and differential reflectivity in weather radars. IEEE Trans. Geosci. Remote Sens. 54, 1727-1737.

Lim, S., Allabakash, S., Jang, B.-J., Chandrasekar, V., 2018. Polarimetric radar signatures of a rare tornado event over south korea. J. Atmos. Oceanic Technol. 35, 1977–1997.

Park, S., Maki, M., Iwanami, K., Bringi, V.N., Chandrasekar, V., 2005. Correction of radar reflectivity and differential reflectivity for rain attenuation at X band. Part II: evaluation and application. J. Atmos. Oceanic Technol. 22, 1633–1655.

Park, H. S., Ryzhkov, A. V., Zrnic´, D. S., 2009. The hydrometeor classification algorithm for the polarimetric WSR-88D: Description and application to an MCS. Wea. Forecasting. 24, 730–748.

Ryzhkov, A., 2007. The impact of beam broadening on the quality of radar polarimetric data. J. Atmos. Oceanic Technol. 24, 729–744.

Ryzhkov, A., Diederich, M., Zhang, P., Simmer, C., 2014. Potential utilization of specific attenuation for rainfall estimation, mitigation of partial beam blockage, and radar networking. J. Atmos. Oceanic Technol. 31, 599–619.

Ryzhkov, A., Zrnic, D., 1998. Beamwidth effects on the differential phase measurements of rain. J. Atmos. Oceanic Technol. 15,624–634.

Schneebeli, M., Grazioli, J., Berne, A., 2014. Improved estimation of the specific differential phase shift using a compilation of Kalman filter ensembles. IEEE Trans. Geosci. Remote Sens. 52(8), 5137-5149.

Schneebeli, M., Berne, A., 2012. An extended Kalman filter framework for polarimetric X-band weather radar data processing. J. Atmos. Oceanic Technol. 29, 711–730.

Shimamura, S., Chandrasekar, V., Ushio, T., Kim, G., Yoshikawa, E., Chen, H., 2016. Probabilistic attenuation correction in a networked radar environment. IEEE Trans. Geosci. Remote Sens. 54,

6930-6939.

Testud, J., Le Bouar, E., Obligis, E., Ali-Mehenni, M., 2000. The rain profiling algorithm applied to polarimetric weather radar. J. Atmos. Oceanic Technol. 17, 332–356.

Trömel, S., Kumjian, M., Ryzhkov, A., Simmer, C., Diederich, M., 2013. Backscatter differential phase: Estimation and variability. J. Appl. Meteor. Climatol. 52, 2529–2548.

Trömel, S., Ryzhkov, A., Zhang, P., Simmer, C., 2014. Investigations of backscatter differential phase in the melting layer. J. Appl. Meteor. Climatol. 53, 2344–2359.

Wang, Y., Chandrasekar, V., 2009. Algorithm for estimation of the specific differential phase, J. Atmos. Ocean. Technol. 26, 2565–2578.

Wen, G., Chen, H., Zhang, G., Sun, J., 2018. An inverse model for raindrop size distribution retrieval with polarimetric variables. Remote Sens. 10, 1179.

Zrnić, D.S., Bringi, V.N., Balakrishnan, N., Aydin, K., Chandrasekar, V., Hubbert, J., 1993. Polarimetric measurements in a severe hailstorm. Mon. Wea. Rev. 121, 2223–2238.

Table Captions:

Table 1. System characteristics of the CPOL radar.

Table 2. Performance scores of four radar derived hourly rainfall products.

Table 3. Performance scores of hourly rainfall accumulations derived from radar (within 100 km coverage).

Table 1. System characteristics of the CPOL radar.

Item	Value
Frequency	5.62GHz
Antenna Diameter	8 m
Antenna Gain	48dB
3 dB Beamwidth	0.46° for elevation 0°, 0.5° and 1.5°; 0.95° for elevation 2.5°, 3.5°, 4.5°, 6.0°, 7.5° and 9°
Polarized Mode	Simultaneous Horizontal and Vertical Polarization (SHV)
Transmitted Peak Power/W	250 Kw
Bandwidth	2 MHz
Noise Figure	3 dB
Dynamic Range	90 dB
Base Data	Original Z_{H}, Z_{H}, V_r, SW, Z_{DR}, ρ_{HV}, Ψ_{DP}, K_{DP}, SNR
Altitude Above Sea Level	1512 m
Max Range for Z_{H}	380 km
Max Range for V_r	230 km
Radial Range Gate Resolution	125 m

Table 2. Performance scores of four radar derived hourly rainfall products.

Range (km)	Gauge total(n)	$R(Z_{\mathrm{H}}^{\mathrm{M}})$			$R(Z_{\mathrm{H}}^{\mathrm{C}})$			$R(Z_{\mathrm{H}}^{\mathrm{M}}, Z_{\mathrm{DR}}^{\mathrm{M}})$			$R(Z_{\mathrm{H}}^{\mathrm{C}}, Z_{\mathrm{DR}}^{\mathrm{C}})$		
		E_{NMA}	E_{RMS}	E_{CC}	E_{NMA}	E_{RMS}	E_{CC}	E_{NMA}	E_{RMS}	E_{CC}	E_{NMA}	E_{RMS}	E_{CC}
[0, 50)	18253	-20.46	5.56	0.85	9.77	3.54	0.92	-38.47	5.65	0.88	-16.26	3.53	0.93
[50,100)	48197	-18.13	4.69	0.82	20.61	3.28	0.91	-36.21	4.70	0.85	-19.75	3.42	0.90
[100,150)	57632	-12.01	3.90	0.75	30.05	3.58	0.84	-37.10	3.92	0.80	-25.74	3.27	0.85
[150,200]	19124	-2.75	3.60	0.77	41.11	3.44	0.85	-31.08	3.52	0.81	-25.62	3.15	0.84

Table 3. Performance scores of hourly rainfall accumulations derived from radar (within coverage range of 100 km).

Score Name	Averaged scores for radar hourly rainfall estimators				
	$R(Z_{\mathrm{H}}^{\mathrm{M}})$	$R(Z_{\mathrm{H}}^{\mathrm{C}})$	$R(Z_{\mathrm{H}}^{\mathrm{M}},\ Z_{\mathrm{DR}}^{\mathrm{M}})$	$(R(Z_{\mathrm{H}}^{\mathrm{C}}, Z_{\mathrm{DR}}^{\mathrm{C}})$	$R(K_{\mathrm{DP}})$
E_{NMA}	0.389	0.347	0.236	0.228	0.188
E_{RMS}(mm)	4.277	3.794	2.561	2.440	2.085
E_{CC}	0.884	0.896	0.943	0.950	0.964

Figure Captions

Fig. 1. (a) The digital elevation map (DEM) information of China; (b) detailed DEM information for the regions indicated by the rectangle in (a), as well as the locations of CPOL radar and HSM radar.

Fig. 2. The radial beam cross sections between HSM and CPOL radars.

Fig. 3. Flowchart of CPOL radar data processing within the framework of ROSE and radar rainfall applications.

Fig. 4. (a) Disdrometer network around the CPOL radar in Hangzhou, China; (b) rain gauge network within the coverage range of 200 km from the CPOL radar. Different colors represent different distance ranges from the radar (black: [0 km, 50 km); red: [50 km, 100 km); blue: [100 km, 150 km); green: [150 km, 200 km]).

Fig. 5. Vertical distribution of polarimetric observables during a "birdbath" scan at 1835UTC, 24 April 2015.

Fig. 6. CPOL radar observations on 0° elevation angle: (a), (c) and (e) are zero-started Ψ_{DP}, $Z_{\mathrm{H}}^{\mathrm{M}}$ and $Z_{\mathrm{DR}}^{\mathrm{M}}$ at 0200 UTC, 01 June 2016, respectively; (b), (d) and (f) are the same with (a), (c) and (e), but at 0200 UTC, 24 June 2017.

Fig. 7. CPOL and HSM radar observations: (a), (c), and (e) are K_{DP}, $Z_{\mathrm{H}}^{\mathrm{C}}$ and $Z_{\mathrm{DR}}^{\mathrm{C}}$ of CPOL radar on 0° elevation angle at 0000 UTC, 01 June 2016, respectively; (g) is the corresponding Z_{H} measurement from the HSM radar on 0.5° elevation angle at 0000 UTC, 01 June 2016. (b), (d), (f) are the same with (a), (c), (e), but at 0001 UTC, 24 June 2017. (h) is the same with (g), but at 2359 UTC, 23 June 2017.

Fig. 8. Comparison of Z_{H} between the HSM and CPOL radars at 0000 UTC, 01 June 2016: (a)-(c) are Z_{H} of the HSM radar, $Z_{\mathrm{H}}^{\mathrm{M}}$ and $Z_{\mathrm{H}}^{\mathrm{C}}$ of the CPOL radar at their common cross sections, respectively; (d) and (e) are the scatter density plots of reflectivity between CPOL radar (before and after attenuation correction) versus HSM radar within their common radial volumes (see Fig. 2).

Fig. 9. Scatter density plots of polarimetric radar measurements simulated from real DSD data collected at eight disdrometer stations during June 2016 and 2017: (a) Z_{DR}vs Z_{H}; (b) K_{DP} vs Z_{H}; (c) $K_{\mathrm{DP}}/Z_{\mathrm{Hl}}$ vs Z_{DR}; (d) and (e) are rainfall rates calculated directly from the DSD versus the simulated Z_{H} and K_{DP}, respectively; (f) is rainfall rates calculated directly from DSD versus the rainfall rate estimates from $R(Z_{\mathrm{H}}, Z_{\mathrm{DR}})$ relation. The black line in (a) represents the fitted Z_{DR}-Z_{H}relation in Eq. (3b). The red lines in (d) and (e) are fitted relations in Eqs. (5b) and (5d), whereas the black lines represent the relations of Eqs. (5c) and (5e).

Fig. 10. Scatter density plots of CPOL radar measurements at 0000 UTC, 01 June 2016: (a) $Z_{\mathrm{DR}}^{\mathrm{M}}$ vs $Z_{\mathrm{H}}^{\mathrm{M}}$; (b) $Z_{\mathrm{DR}}^{\mathrm{C}}$ vs $Z_{\mathrm{H}}^{\mathrm{C}}$; (c) K_{DP} vs $Z_{\mathrm{H}}^{\mathrm{M}}$; (d) K_{DP} vs $Z_{\mathrm{H}}^{\mathrm{C}}$; (e) $K_{\mathrm{DP}}/Z_{\mathrm{Hl}}^{\mathrm{M}}$ vs $Z_{\mathrm{DR}}^{\mathrm{M}}$; (f) $K_{\mathrm{DP}}/Z_{\mathrm{Hl}}^{\mathrm{C}}$

vs Z_{DR}^{C}. $Z_{\mathrm{Hl}}^{\mathrm{M}}$ and $Z_{\mathrm{Hl}}^{\mathrm{C}}$ are linear scale ($\mathrm{mm}^6 \cdot \mathrm{mm}^{-3}$) reflectivity before and after attenuation, respectively.

Fig. 11. The same as Fig. 10, but at 0001 UTC, 24 June 2017.

Fig. 12. Scatter density plots of radar-derived hourly rainfall estimates: (a), (b), (c) and (d) denote $R(Z_{\mathrm{H}}^{\mathrm{M}})$ vs $R(Z_{\mathrm{H}}^{\mathrm{C}})$ within the coverage range of [0 km, 50km), [50km,100km), [100km,150km) and [150km,200km], respectively; (e)-(h) are the same with (a)-(d), but for $R(Z_{\mathrm{H}}^{\mathrm{M}}, Z_{\mathrm{DR}}^{\mathrm{M}})$ vs $R(Z_{\mathrm{H}}^{\mathrm{C}}, Z_{\mathrm{DR}}^{\mathrm{C}})$.

Fig. 13. Scatter density plots of radar-derived hourly rainfall estimates using $R(Z_{\mathrm{H}})$ versus rain gauge measurements: (a), (b), (c) and (d) are all based on $R(Z_{\mathrm{H}}^{\mathrm{M}})$ within the coverage range of [0 km, 50km), [50km,100km), [100km,150km) and [150km,200km), respectively. (e)-(h) are the same with (a)-(d), but based on $R(Z_{\mathrm{H}}^{\mathrm{C}})$.

Fig. 14. Scatter density plots of radar-derived hourly rainfall estimates using $R(Z_{\mathrm{H}}, Z_{\mathrm{DR}})$ versus rain gauge measurements: (a), (b), (c) and (d) are all based on $R(Z_{\mathrm{H}}^{\mathrm{M}}, Z_{\mathrm{DR}}^{\mathrm{M}})$ within the coverage range of [0 km, 50km), [50km,100km), [100km,150km) and [150km,200km], respectively. (e)-(h) are the same with (a)-(d), but based on $R(Z_{\mathrm{H}}^{\mathrm{C}}, Z_{\mathrm{DR}}^{\mathrm{C}})$.

Fig. 15. Two parts of the $R(Z_{\mathrm{H}}, Z_{\mathrm{DR}})$ relationship: (a) represents the Z_{H}-related part, while (b) is the Z_{DR}-related part.

Fig. 16. Scatter density plots of hourly rainfall estimates within the coverage of 100 km from CPOL radar: (a) radar estimates using $R(K_{\mathrm{DP}})$ vs rain gauge measurements; (b) radar estimates using $R(Z_{\mathrm{H}}^{\mathrm{M}})$ vs $R(K_{\mathrm{DP}})$; (c) radar estimates using $R(Z_{\mathrm{H}}^{\mathrm{M}}, Z_{\mathrm{DR}}^{\mathrm{M}})$ vs $R(K_{\mathrm{DP}})$; (d) radar estimates using $R(Z_{\mathrm{H}}^{\mathrm{C}}, Z_{\mathrm{DR}}^{\mathrm{C}})$ vs $R(Z_{\mathrm{H}}^{\mathrm{C}})$; (e) radar estimates using $R(Z_{\mathrm{H}}^{\mathrm{C}})$ vs $R(K_{\mathrm{DP}})$; (f) radar estimates using $R(Z_{\mathrm{H}}^{\mathrm{C}}, Z_{\mathrm{DR}}^{\mathrm{C}})$ vs $R(K_{\mathrm{DP}})$.

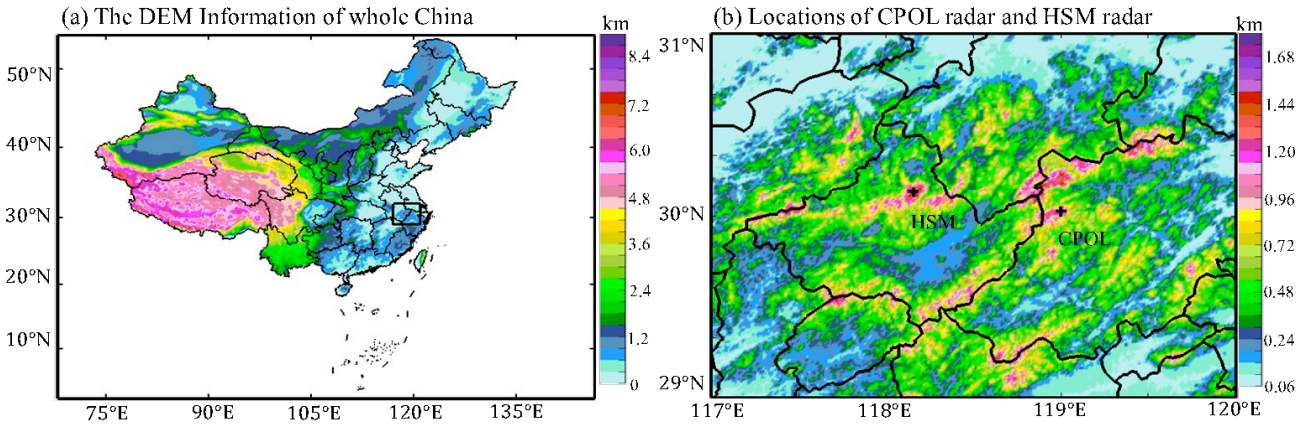

Fig. 1. (a) The digital elevation map (DEM) information of China; (b) detailed DEM information for the regions indicated by the rectangle in (a), as well as the locations of CPOL radar and HSM radar.

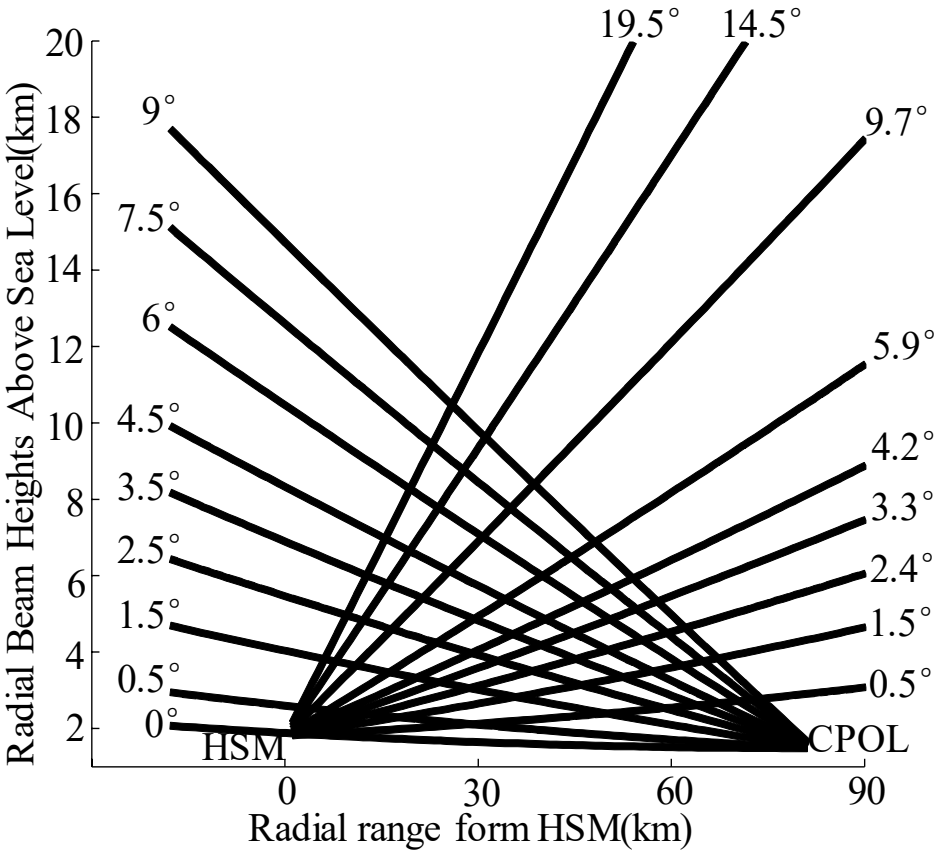

Fig. 2. The radial beam cross sections between HSM and CPOL radars.

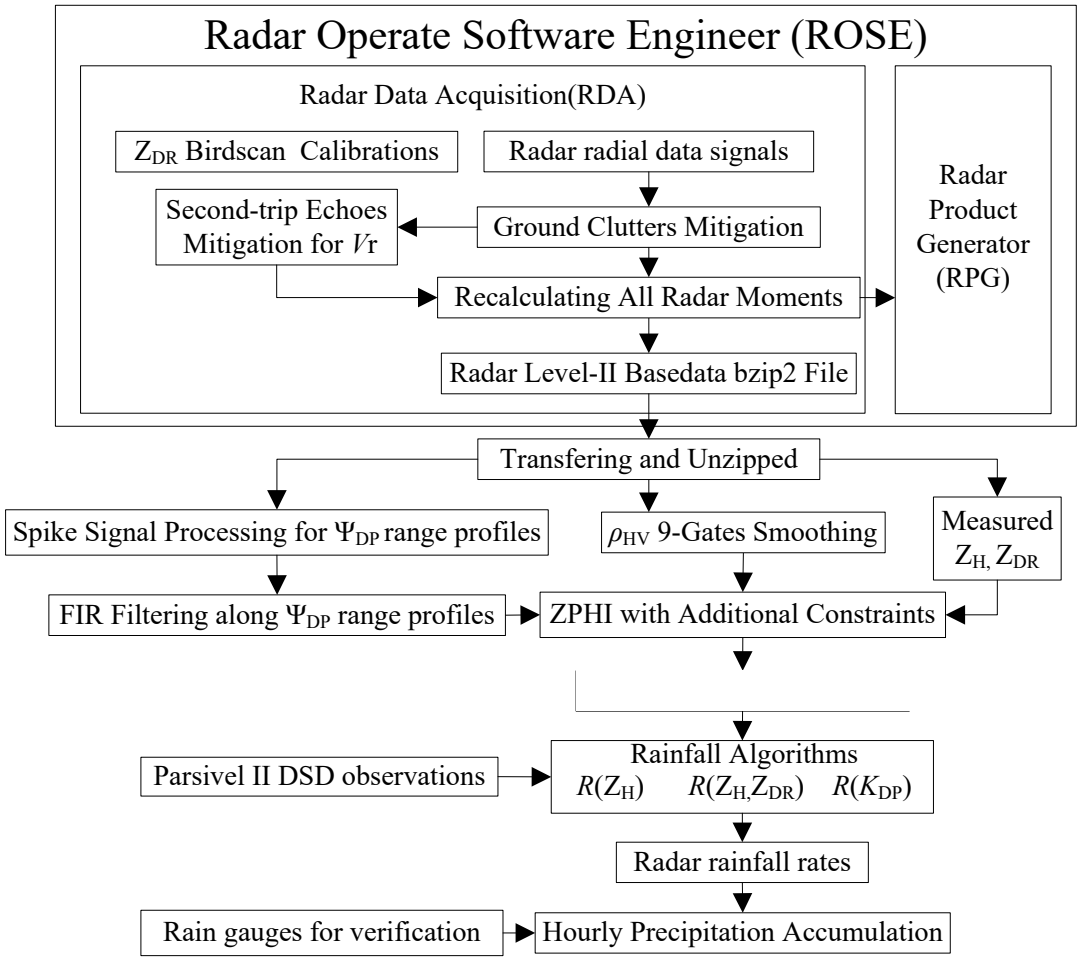

Fig. 3. Flowchart of CPOL radar data processing within the framework of ROSE and radar rainfall applications.

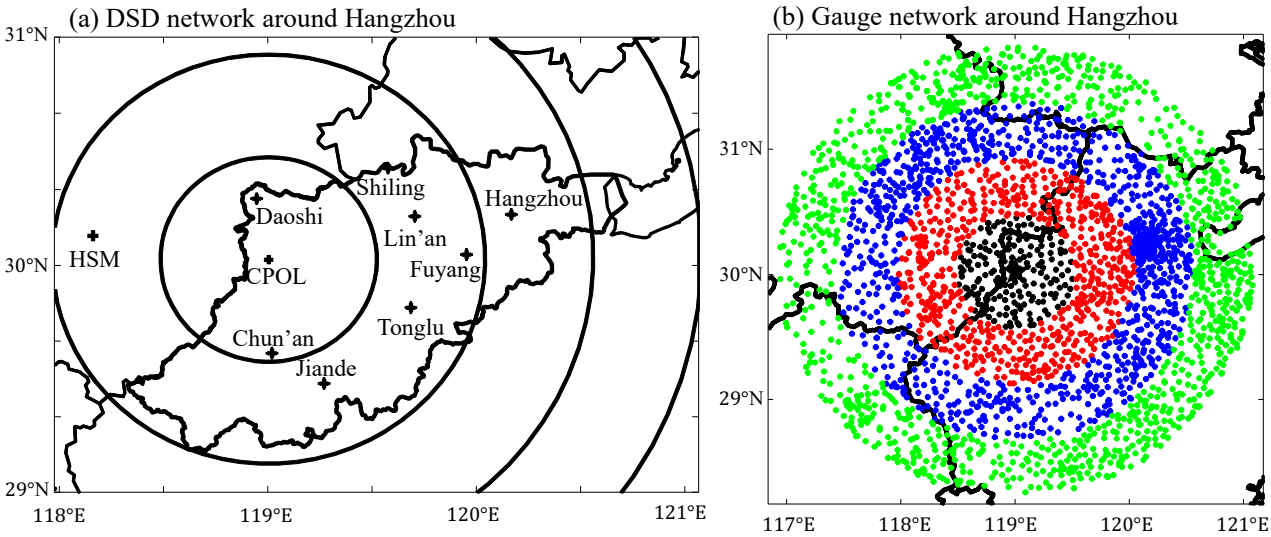

Fig. 4. (a) Disdrometer network around the CPOL radar in Hangzhou, China; (b) rain gauge network within the coverage range of 200 km from the CPOL radar. Different colors represent different distance ranges from the radar (black: [0 km, 50 km); red: [50 km, 100 km); blue: [100 km, 150 km); green: [150 km, 200 km]).

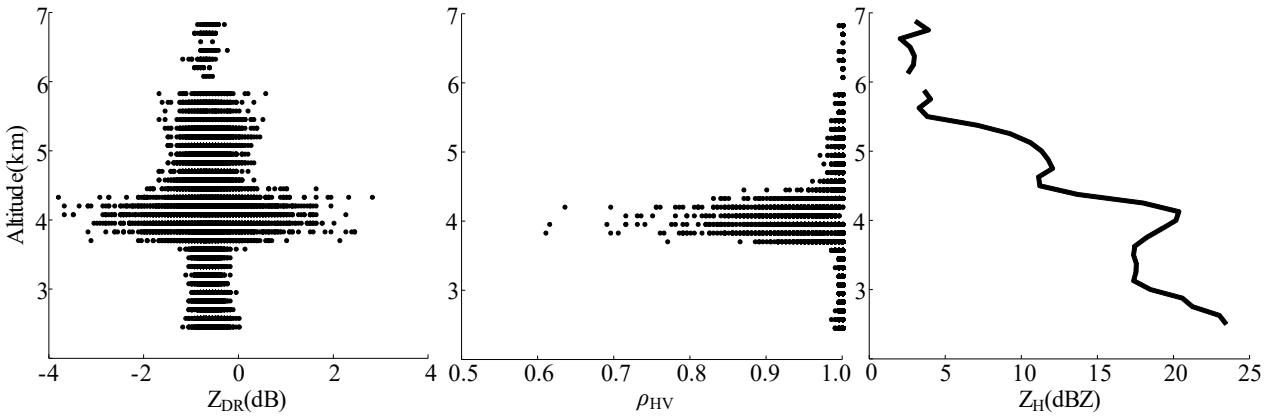

Fig. 5. Vertical distribution of polarimetric observables during a "birdbath" scan at 1835UTC, 24 April 2015.

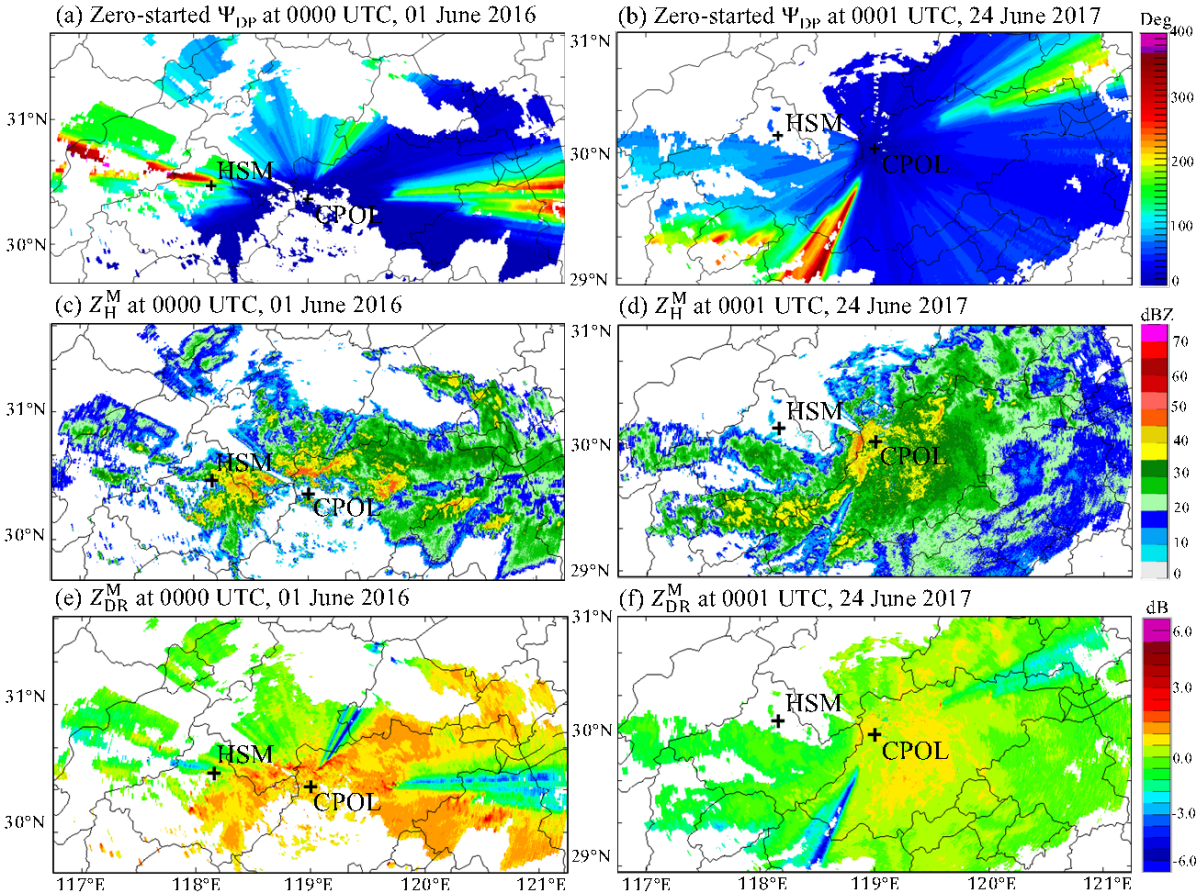

Fig. 6. CPOL radar observations on 0° elevation angle: (a), (c) and (e) are zero-started Ψ_{DP}, Z_H^M and Z_{DR}^M at 0200 UTC, 01 June 2016, respectively; (b), (d) and (f) are the same with (a), (c) and (e), but at 0200 UTC, 24 June 2017.

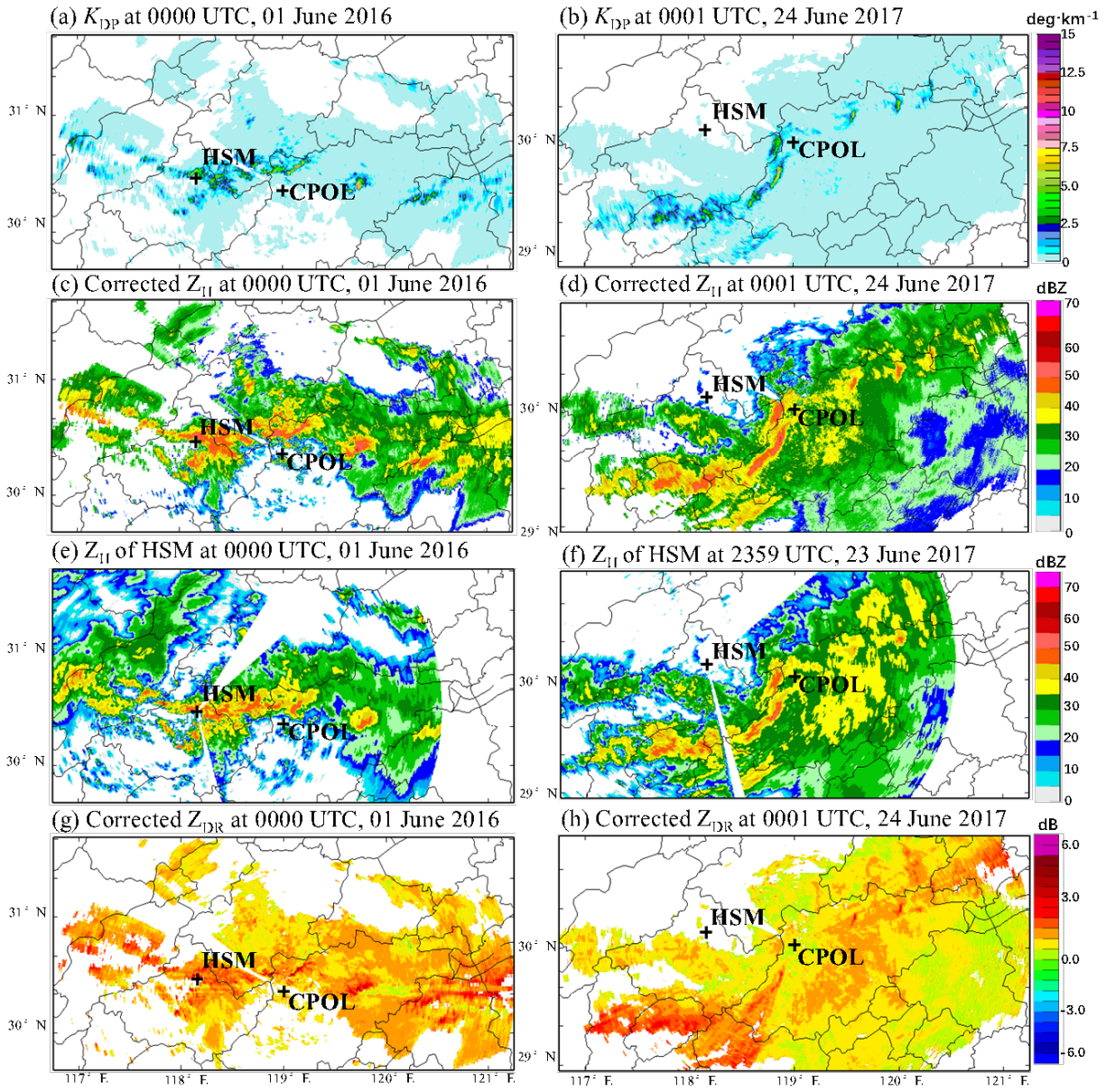

Fig. 7. CPOL and HSM radar observations: (a), (c), and (e) are K_{DP}, Z_H^C and Z_{DR}^C of CPOL radar on 0° elevation angle at 0000 UTC, 01 June 2016, respectively; (g) is the corresponding Z_H measurement from the HSM radar on 0.5° elevation angle at 0000 UTC, 01 June 2016. (b), (d), (f) are the same with (a), (c), (e), but at 0001 UTC, 24 June 2017. (h) is the same with (g), but at 2359 UTC, 23 June 2017.

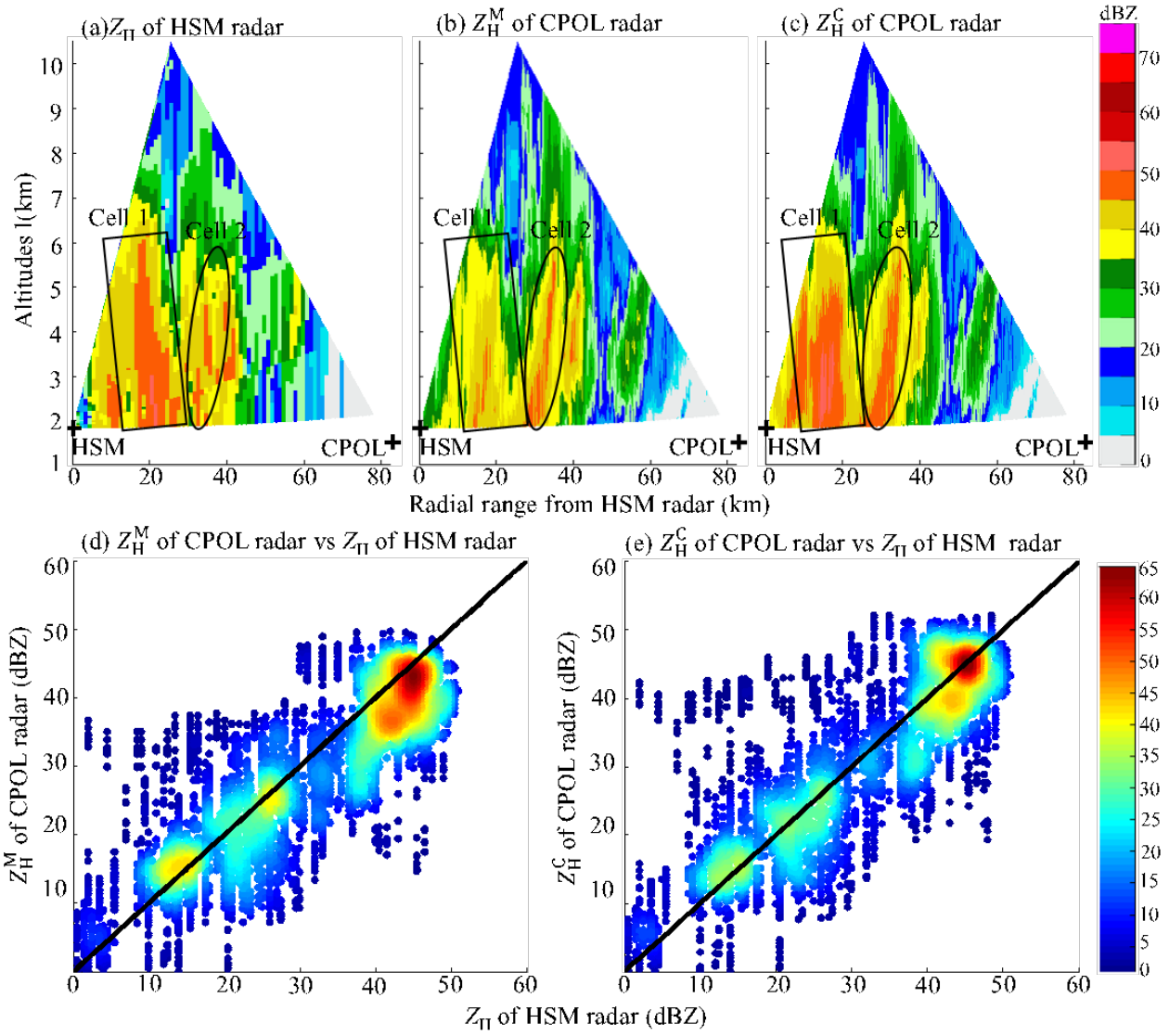

Fig. 8. Comparison of Z_H between the HSM and CPOL radars at 0000 UTC, 01 June 2016: (a)-(c) are Z_H of the HSM radar, Z_H^M and Z_H^C of the CPOL radar at their common cross sections; (d) and (e) are the scatter density plots of reflectivity between CPOL radar (before and after attenuation correction) versus HSM radar within their common radial volumes (see Fig. 2).

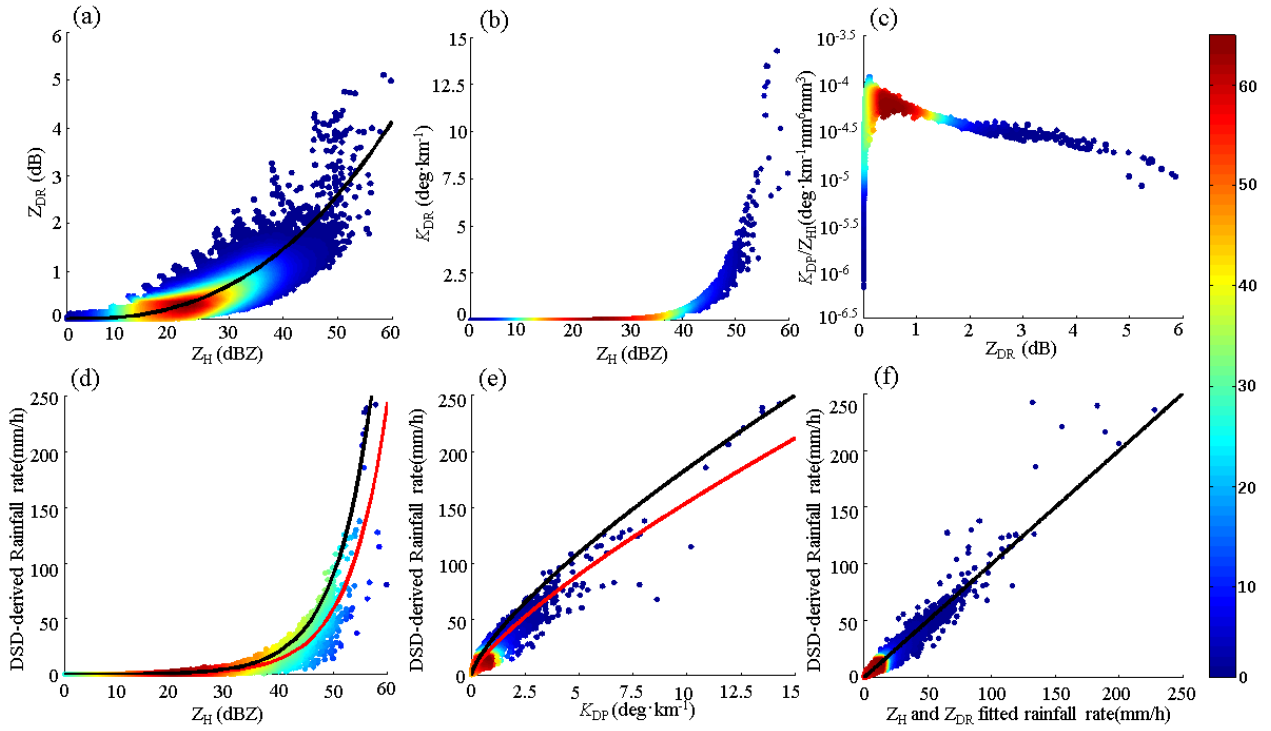

Fig. 9. Scatter density plots of polarimetric radar measurements simulated from real DSD data collected at eight disdrometer stations during June 2016 and 2017: (a) Z_{DR}vs Z_{H}; (b) K_{DP} vs Z_{H}; (c) $K_{\mathrm{DP}}/Z_{\mathrm{H}}$vs Z_{DR}; (d) and (e) are rainfall rates calculated directly from the DSD versus the simulated Z_{H} and K_{DP}, respectively. (f) is rainfall rates calculated directly from DSD versus the rainfall rate estimates from $R(Z_{\mathrm{H}}, Z_{\mathrm{DR}})$ relation. The black line in (a) represents the fitted $Z_{\mathrm{DR}} - Z_{\mathrm{H}}$ relation in Eq. (3b). The red lines in (d) and (e) are fitted relations of Eqs. (5b) and (5d), whereas the black lines represent the relations of Eqs. (5c) and (5e).

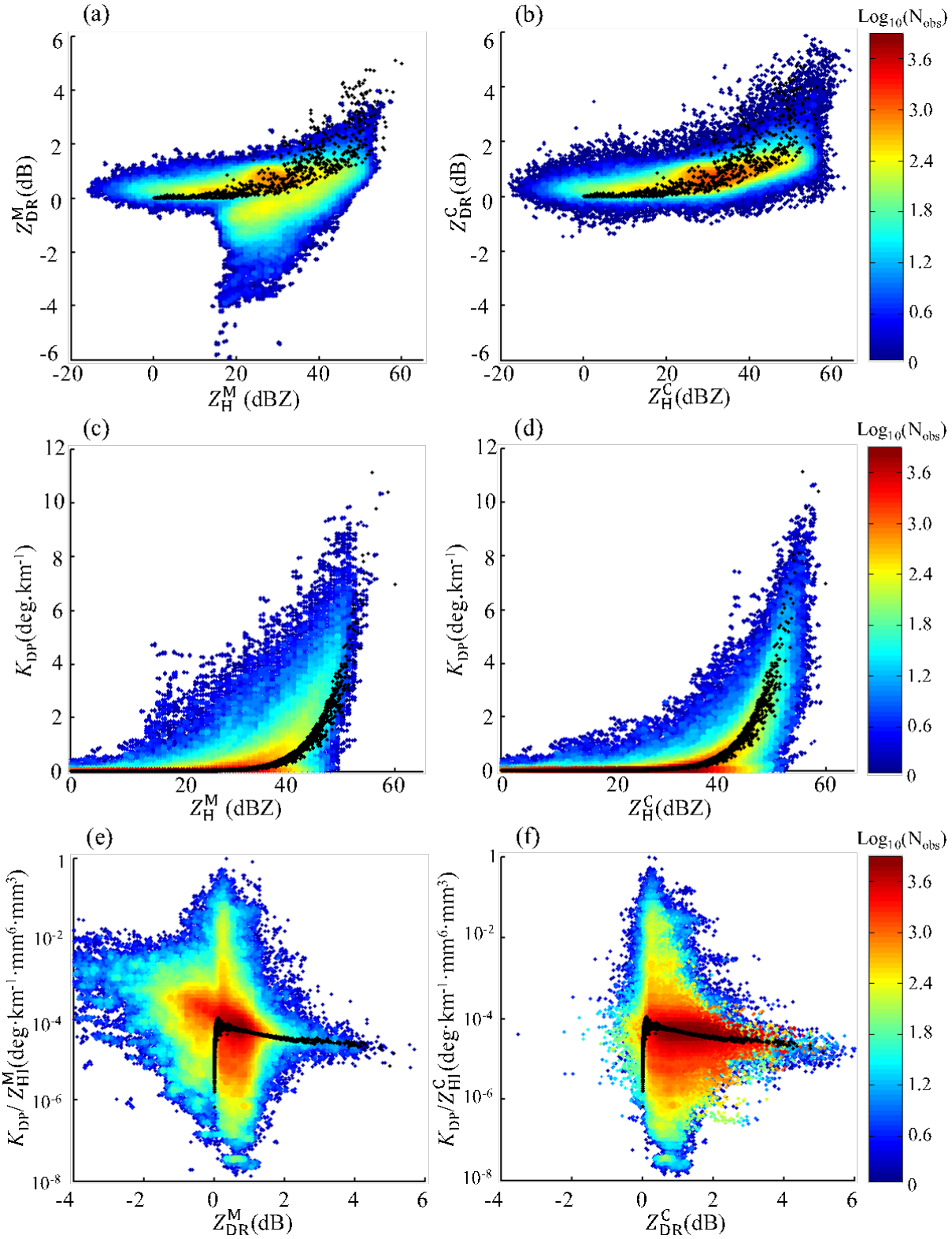

Fig. 10. Scatter density plots of CPOL radar measurements at 0000 UTC, 01 June 2016: (a) $Z_{\mathrm{DR}}^{\mathrm{M}}$ vs $Z_{\mathrm{H}}^{\mathrm{M}}$; (b) $Z_{\mathrm{DR}}^{\mathrm{C}}$ vs $Z_{\mathrm{H}}^{\mathrm{C}}$; (c) K_{DP} vs $Z_{\mathrm{H}}^{\mathrm{M}}$; (d) K_{DP} vs $Z_{\mathrm{H}}^{\mathrm{C}}$; (e) $K_{\mathrm{DP}}/Z_{\mathrm{HI}}^{\mathrm{M}}$ vs $Z_{\mathrm{DR}}^{\mathrm{M}}$; (f) $K_{\mathrm{DP}}/Z_{\mathrm{HI}}^{\mathrm{C}}$ vs Z_{DR}^{C}. $Z_{\mathrm{HI}}^{\mathrm{M}}$ and $Z_{\mathrm{HI}}^{\mathrm{C}}$ are linear scale (mm^{6}·m^{-3}) reflectivity before and after attenuation, respectively.

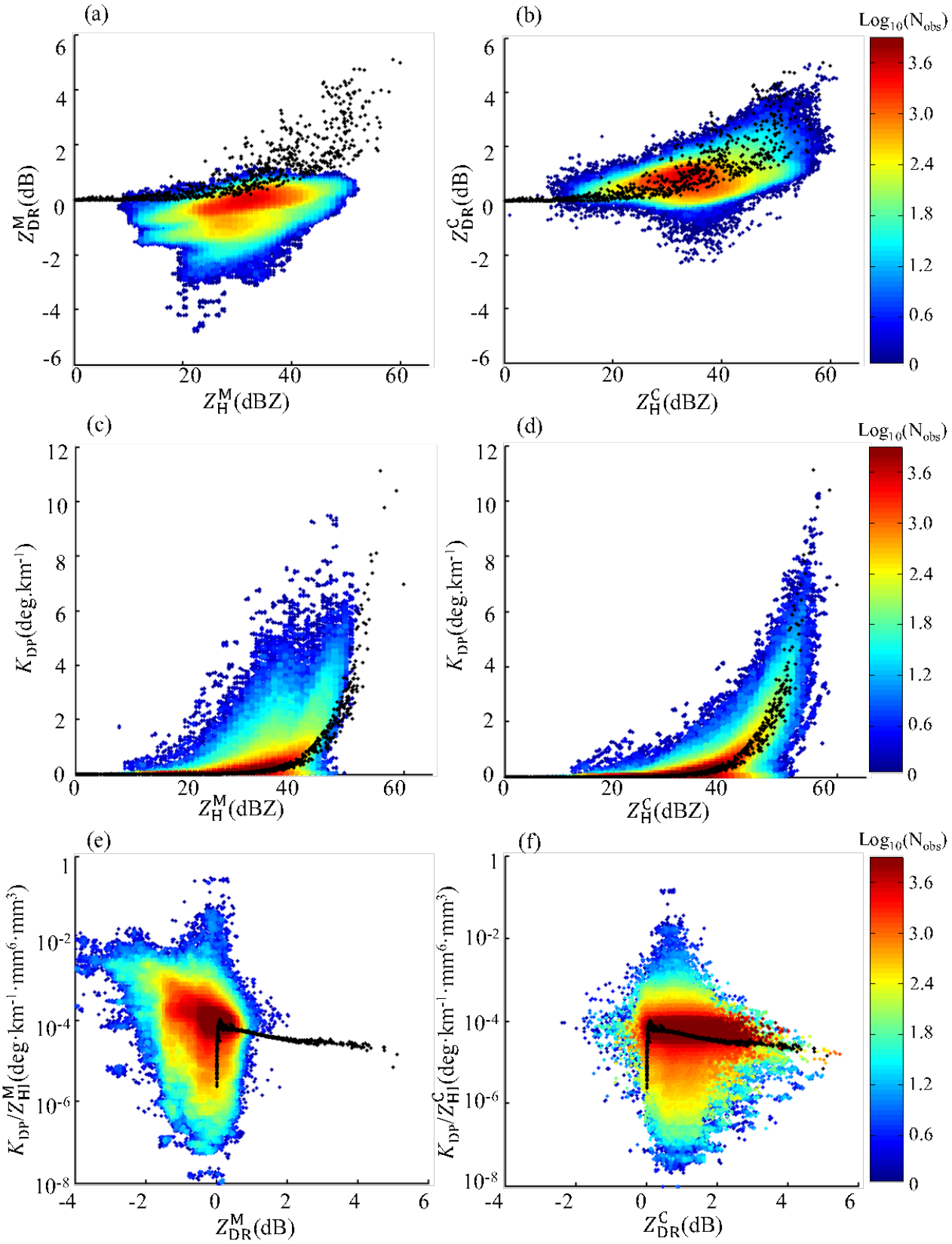

Fig. 11. The same as Fig. 10, but at 0001 UTC, 24 June 2017.

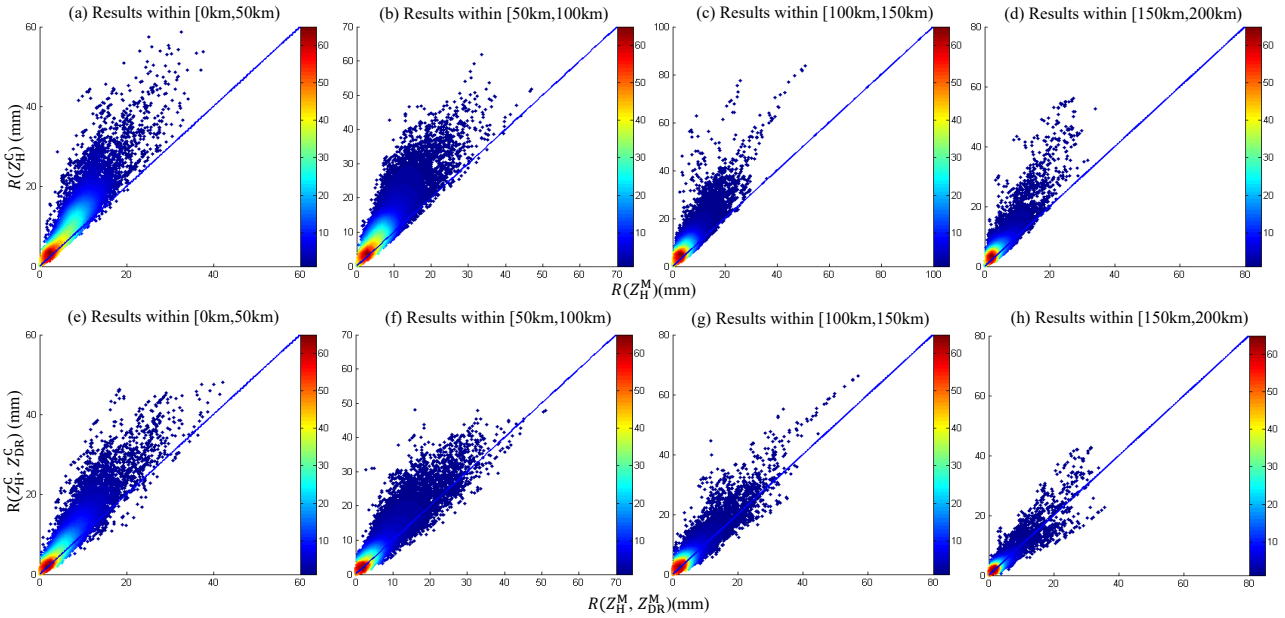

Fig. 12. Scatter density plots of radar-derived hourly rainfall estimates: (a), (b), (c) and (d) denote $R(Z_{\mathrm{H}}^{\mathrm{M}})$ vs $R(Z_{\mathrm{H}}^{\mathrm{C}})$ within the coverage range of [0 km, 50km), [50km,100km), [100km,150km) and [150km, 200km], respectively; (e)-(h) are the same with (a)-(d), but for $R(Z_{\mathrm{H}}^{\mathrm{M}}, Z_{\mathrm{DR}}^{\mathrm{M}})$ vs $R(Z_{\mathrm{H}}^{\mathrm{C}}, Z_{\mathrm{DR}}^{\mathrm{C}})$.

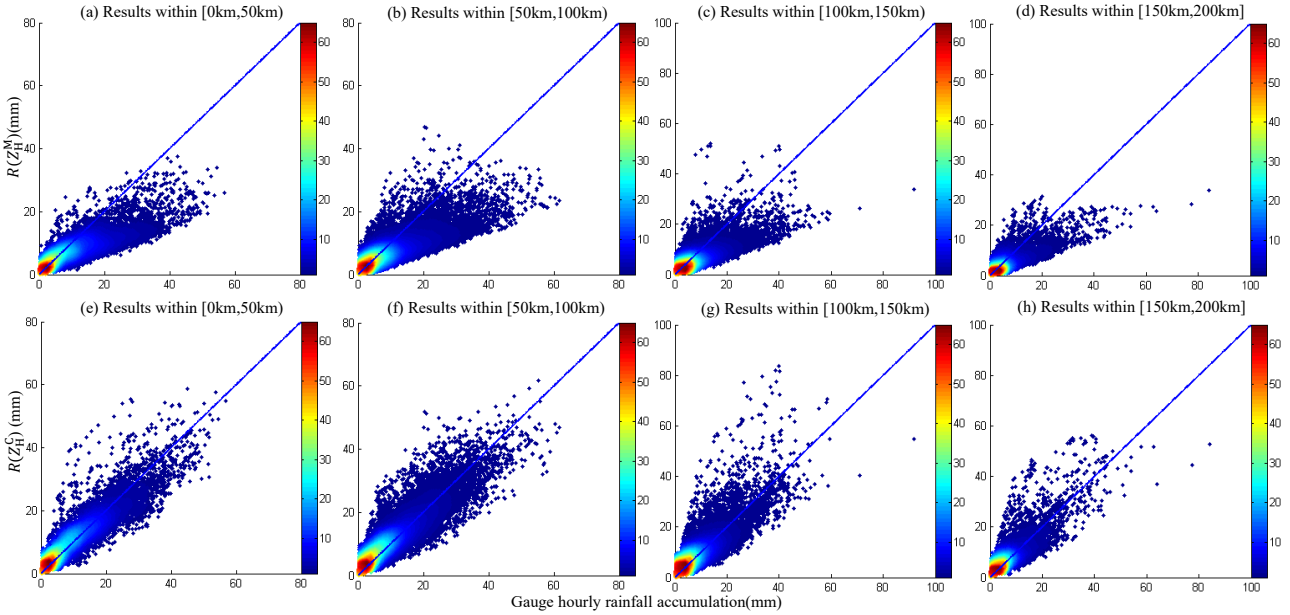

Fig. 13. Scatter density plots of radar-derived hourly rainfall estimates using $R(Z_H)$ versus rain gauge measurements: (a), (b), (c) and (d) are respectively based on $R(Z_H^M)$ within the coverage range of [0 km, 50km), [50km,100km), [100km,150km) and [150km,200km); (e)-(h) are the same with (a)-(d), but based on $R(Z_H^C)$.

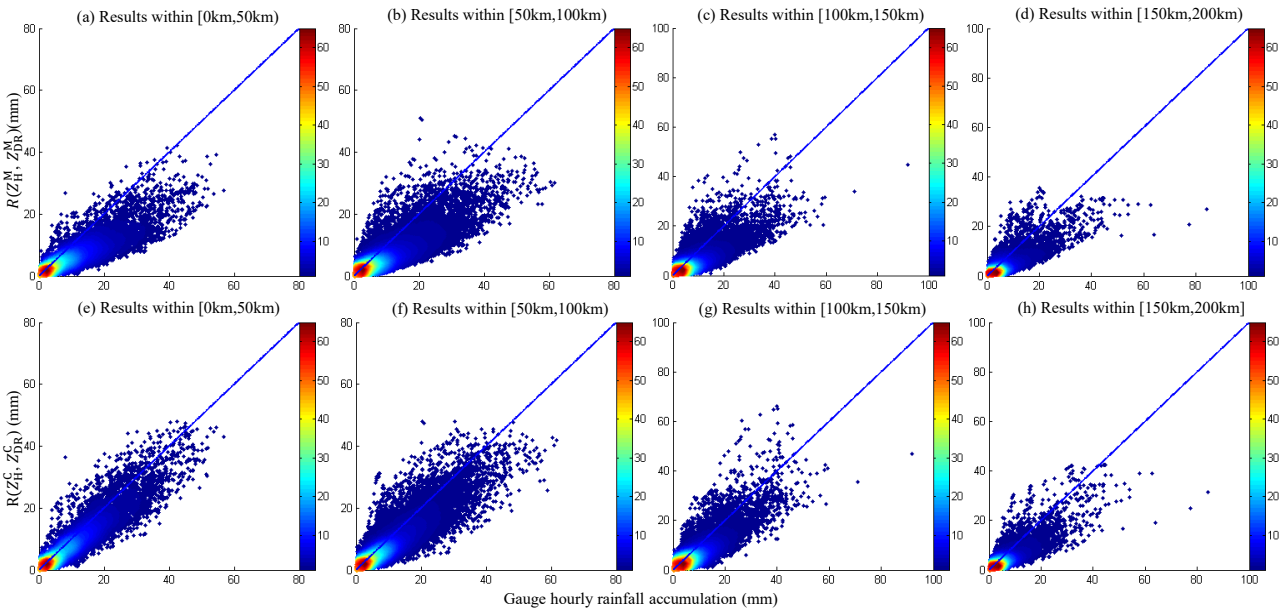

Fig. 14. Scatter density plots of radar-derived hourly rainfall estimates using $R(Z_{\mathrm{H}}, Z_{\mathrm{DR}})$ versus rain gauge measurements: (a), (b), (c) and (d) are respectively based on $R(Z_{\mathrm{H}}^{\mathrm{M}}, Z_{\mathrm{DR}}^{\mathrm{M}})$ within the coverage range of [0 km, 50km), [50km,100km), [100km,150km) and [150km,200km]. (e)-(h) are the same with (a)-(d), but based on $R(Z_{\mathrm{H}}^{\mathrm{C}}, Z_{\mathrm{DR}}^{\mathrm{C}})$.

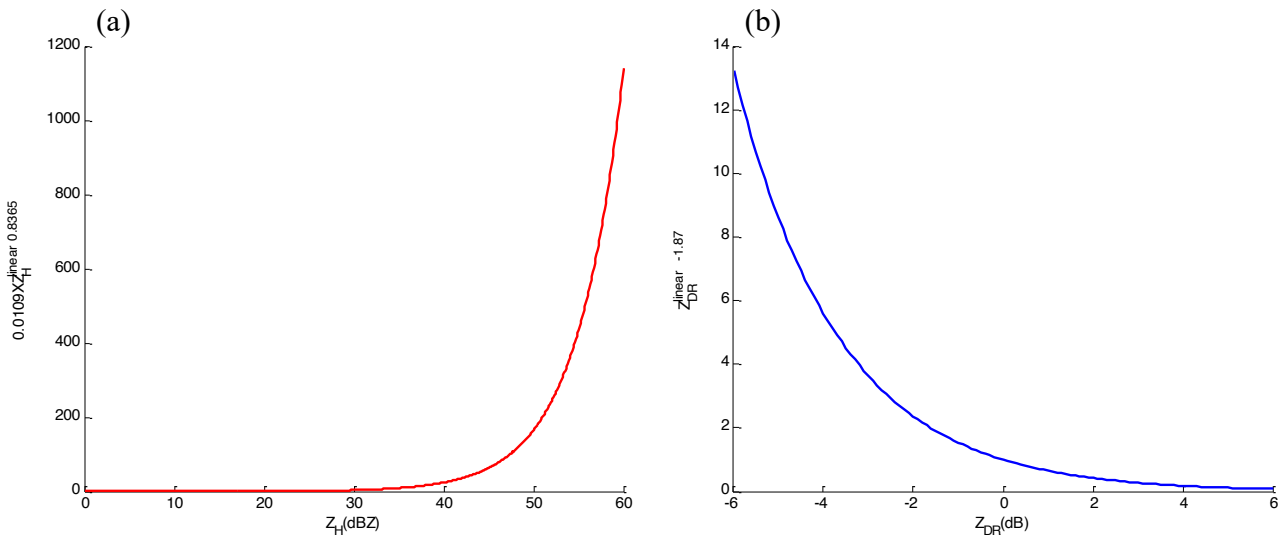

Fig. 15. Two parts of the $R(Z_{\mathrm{H}}, Z_{\mathrm{DR}})$ relationship: (a) represents the Z_{H}-related part, while (b) is the Z_{DR}-related part.

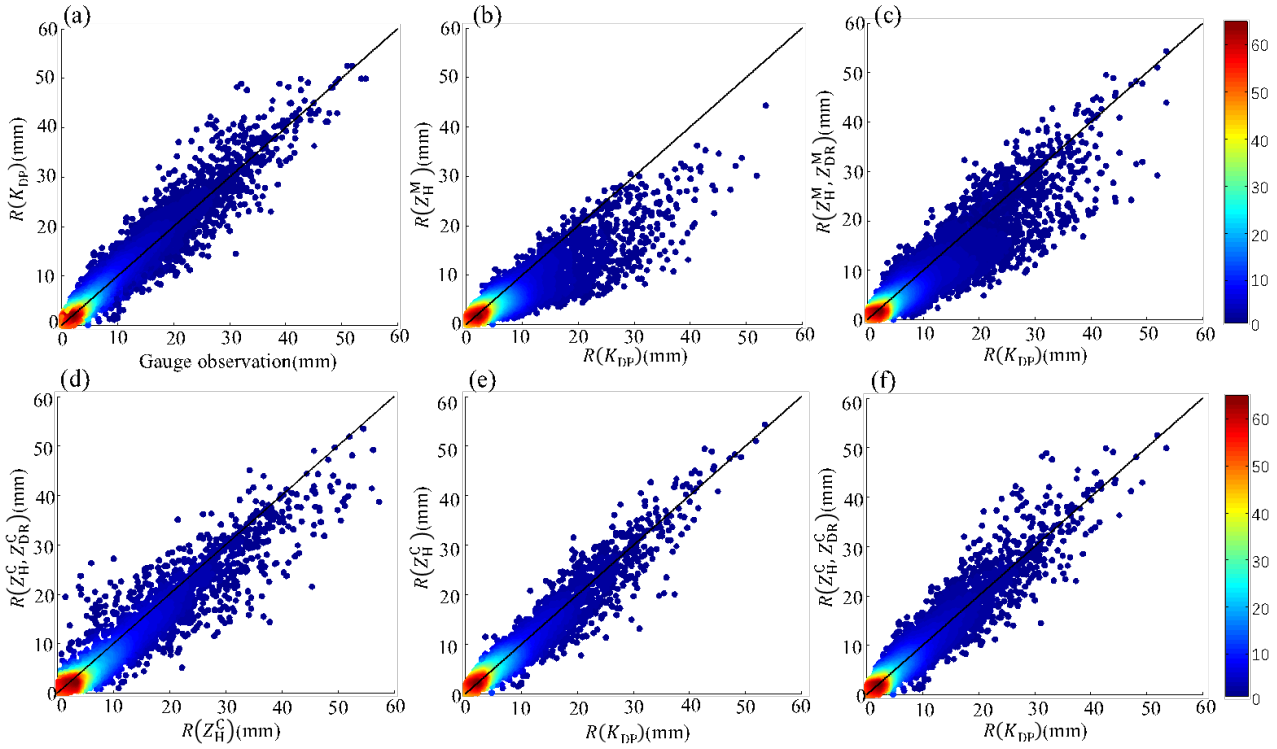

Fig. 16. Scatter density plots of hourly rainfall estimates within the coverage of 100 km from CPOL radar: (a) radar estimates using $R(K_{DP})$ vs rain gauge measurements; (b) radar estimates using $R(Z_H^M)$ vs $R(K_{DP})$; (c) radar estimates using $R(Z_H^M, Z_{DR}^M)$ vs $R(K_{DP})$; (d) radar estimates using $R(Z_H^C, Z_{DR}^C)$ vs $R(Z_H^C)$; (e) radar estimates using $R(Z_H^C)$ vs $R(K_{DP})$; (f) radar estimates using $R(Z_H^C, Z_{DR}^C)$ vs $R(K_{DP})$.